

The optical absorption in indirect semiconductor to semimetal PtSe₂ arises from direct transitions

Marin Tharrault,¹ Sabrine Ayari,¹ Mehdi Arfaoui,² Eva Desgué,³ Romaric Le Goff,¹ Pascal Morfin,¹ José Palomo,¹ Michael Rosticher,¹ Sihem Jaziri,^{2,4} Bernard Plaçais,¹ Pierre Legagneux,³ Francesca Carosella,¹ Christophe Voisin,¹ Robson Ferreira,¹ and Emmanuel Baudin^{1,5}

¹*Laboratoire de Physique de l'Ecole normale supérieure, ENS, Université PSL, CNRS, Sorbonne Université, Université de Paris, 24 rue Lhomond, 75005 Paris, France*

²*Laboratoire de Physique de la Matière Condensée, Faculté des Sciences de Tunis, Université Tunis El Manar, Campus Universitaire 1060 Tunis, Tunisia.*

³*Thales Research & Technology, 91767 Palaiseau, France*

⁴*Laboratoire de Physique des Matériaux : Structure et Propriétés, Faculté des Sciences de Bizerte, Université de Carthage, 7021 Jarzouna, Tunisia.*

⁵*Institut universitaire de France*

Abstract

PtSe₂ is a van der Waals material transitioning from an indirect bandgap semiconductor to a semimetal with increasing thickness. Its absorption threshold has been conjectured to originate from interband indirect transitions. By quantitative comparison between broadband (0.8 – 3.0 eV) optical absorption of high-quality exfoliated crystals and DFT *ab initio* simulations, we prove instead that the optical absorption arises only from direct transitions. This understanding allows us to shed light on the semiconductor-to-semimetal transition and to explore the effect of stacking and excitons on the optical absorption.

Two-dimensional materials are promising candidates for the future of high-speed optoelectronics, owing to their large electronic mobilities, strong light-matter coupling, and intrinsically low carrier densities [1, 2]. The near-infrared telecommunication band (0.8 – 1.0 eV) is particularly relevant to optoelectronic applications in information technology. However, only a few 2D materials can operate in this range, specifically the family of noble transition metal dichalcogenides (NTMDs) [3, 4]. Indeed, unlike other 2D materials, NTMDs exhibit a widely tunable bandgap with layer number, giving the possibility to target a desired wavelength range. Among them, Platinum Diselenide (PtSe₂) has raised significant interest due to its air stability, and to the availability of scalable methods to produce high-quality grown films [5–7]. PtSe₂ features an indirect bandgap above 1 eV in its monolayer form and undergoes a transition to a semimetal as the number of stacked layers increases [8–10]. Yet, the light absorption mechanism on which photodetection processes rely is largely misunderstood.

Such issues are not uncommon when dealing with newly discovered materials. In the 1990s, there was an intense debate regarding the nature of the optical bandgap of carbon nanotubes, which was eventually resolved by the demonstration of its excitonic origin [11]. In PtSe₂, the near-infrared (NIR) absorption tail has been presumed to originate from indirect interband transitions [8, 12–22] – as it is the case for bulk indirect bandgap semiconductors (e.g., Silicon) – and some studies have hypothesized the involvement of bound excitons in its optical absorption peaks [23–25].

In this letter, we demonstrate instead that the optical absorption of PtSe₂ in the near-infrared to visible (NIR-vis) range is driven by single-electron direct optical transitions, irrespective of the material semimetallic or semiconducting nature. Our conclusion is supported by a body of consistent experimental and theoretical evidence. The mechanism of optical absorption is elucidated through quantitative agreement between micro-absorption spectroscopy of intrinsic exfoliated layer-defined

PtSe₂ flakes and DFT-based (density functional theory) optical absorption calculation, over the NIR-vis spectral range (0.8 – 3.0 eV). Alternative explanations are ruled out by studying the dependence of optical absorption with temperature and material quality. Moreover, understanding NIR-vis optical absorption enables the determination of the number of layers for which PtSe₂ transits from a semiconductor to a semimetal – crucial for photodetection applications. It also allows us to investigate the impact of layer stacking and bound excitons on optical absorption.

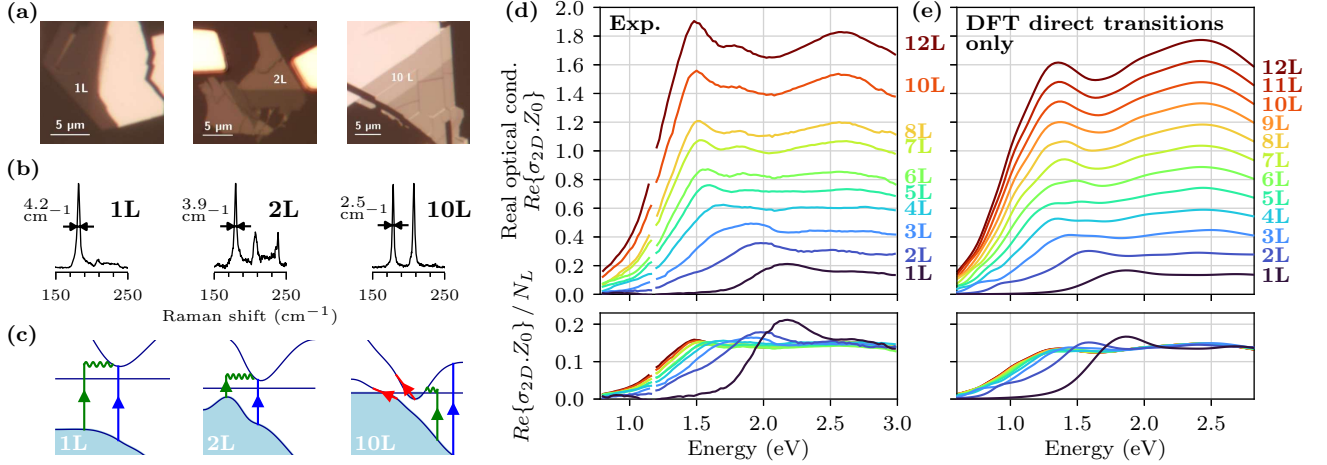


FIG. 1. Optical absorption of PtSe₂ exfoliated flakes. (a) Microscope images on fused silica under white lamp illumination in reflection, (b) Raman spectra (with E_g mode linewidth) and (c) schematic of photon absorption mechanisms under consideration for 1L, 2L and 10L flakes (the horizontal line is the Fermi level) – depicting intraband (red), indirect interband (green) and direct interband (blue) transitions. (d) Experimental and (e) theoretical real 2D optical conductivities $Re\{\sigma_{2D} \cdot Z_0\}$ (top plots), and their values normalized by the layers count N_L (bottom plots). $Z_0 = 377 \Omega$ is the impedance of free space.

PtSe₂ samples are peeled from crystals grown by chemical vapor transport (HQ graphene) using Au-assisted mechanical exfoliation [26, 27], and transferred onto fused silica substrates (Fig. 1a, see also SM-1). The monolayer to multilayers PtSe₂ flakes feature the characteristic Raman signatures of the octahedral phase [28] (Fig. 1b). The E_g Raman peaks have narrow linewidths, testifying of the high crystallinity of the exfoliated material. These samples have been the subject of a detailed Raman study in reference [29].

We use a high-accuracy NIR-vis (0.8 – 3.0 eV) micro-absorption setup at room temperature to study the exfoliated PtSe₂ flakes. The acquisition of both reflectance and transmittance enables the determination of the complex two-dimensional optical conductivity (SM-3). For thin films, its

real component (Fig. 1d) is simply the optical absorption in vacuum [30]. The optical spectra feature a plateau on the blue side (2.5 – 3.0 eV, Fig. 1d), and show a slowly decaying tail on the infrared side. This high-energy plateau allows identifying the number of layers by using the linear scaling of the real 2D optical conductivity with layer count (Fig. 1d, bottom plot). This method is consistent with atomic force microscopy thickness measurements (in combination with Raman spectroscopy, SM-2). Two dominant peaks can be distinguished (at 1.5 eV and 2.6 eV for the thick samples), which redshift with increasing thickness. This effect is common in 2D semiconductors [31], but is particularly pronounced in PtSe₂, due to its strong interlayer interaction. The tail decay extends over an energy range 20 times larger than the thermal energy and so cannot be attributed to thermal broadening of the main absorption peak. Interestingly, as the material transits from an indirect semiconductor to a semimetal with increasing thickness – within the 3L - 10L range [9, 32–36] – no semimetallic signature emerges in the infrared part of the absorption spectrum.

Several mechanisms can be responsible for the NIR-vis optical absorption: intraband transitions, indirect interband transitions, and direct interband transitions (Fig. 1c) [37]. Semimetallic PtSe₂ shows free-electron signatures in the THz range [22, 38, 39] but the absorption driven by intraband transitions can be neglected at optical frequencies.

Owing to the indirect nature of the bandgap, and to the slow decay of the NIR absorption tail, previous works studying optical absorption conjectured that indirect optical transitions are responsible for PtSe₂ infrared absorption [8, 12–22], and extracted indirect bandgaps using the Tauc model for indirect bandgap semiconductors [40]. However, it is well-known that in indirect semiconductors as silicon and germanium, the high-energy optical absorption is dominated by direct transitions, and orders of magnitude smaller indirect transitions are only revealed below the direct optical bandgap [41]. We therefore compare the experimental spectra with the optical absorption deduced from DFT simulation, only considering direct optical transitions (Fig. 1e). DFT computation relies on the GGA-IPA method for an AA-stacked octahedral PtSe₂ structure (SM-4). We obtain a remarkable quantitative agreement between the simulated and measured absorption magnitudes. Additionally, the absorption profiles feature similar absorption peaks and low-energy absorption tails. This striking correspondence strongly indicates that the direct transition mechanism dominates the optical response. This interpretation is more thoroughly developed below.

Let us consider the origin of the optical absorption specific features, starting with the main absorption peaks. Several works [24, 25] attributed these peaks to bound excitons. By analyzing

the simulated optical absorption in detail, we see that these peaks originate instead from band nested direct transitions. To demonstrate this point, let us focus on the simplest cases of monolayer and bilayer PtSe₂.

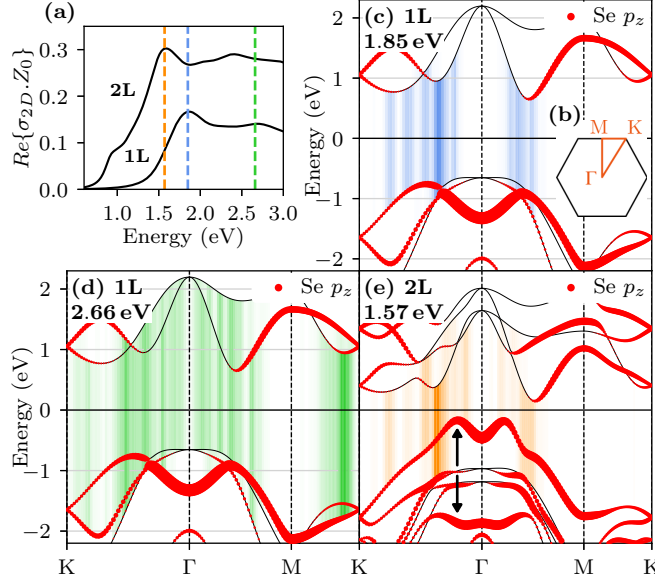


FIG. 2. Contributions to the optical absorption peaks. (a) DFT-computed optical absorption of 1L and 2L. (b) (Irreducible) Brillouin zone in (orange) black. (c-e) Optical absorption contributions at given energies (dashed lines in (a)), for 1L and 2L absorption peaks, decomposed on the electronic band structure plotted along the K- Γ -M-K direction. Colored lines with varying opacity illustrate the relative contribution of pairs of eigenstates to the optical absorption. The selenium p_z orbital component is displayed in red, the line thickness giving its magnitude.

Our numerical method allows to isolate the bands and k-wavevectors that contribute the most to the optical absorption for a given photon energy. The 1.85 eV and 1.57 eV absorption peaks of 1L and 2L arise from optical transitions located around the center of the irreducible Brillouin zone (Fig. 2a, b, c, e). These transitions involve locally parallel valence and conduction bands, leading to local enhancements in the joint density of state (SM-5a), and consequently to optical absorption peaks – a situation known as the band nesting effect [42]. These peaks arise from optically active transitions from the symmetric selenium p_z^+ orbital to the platinum $d_{x^2-y^2/xy}$ orbital (SM-4e). Similarly, the 2.66 eV absorption peak of 1L originates from nesting of bands between the M and K points (Fig. 2d) and involves the Se $p_{x/y}^+$ and Pt $d_{zx/zy}$ orbitals.

For two stacked monolayers, the interlayer hybridization is particularly strong for states com-

posed of an important selenium p_z orbital component (Fig. 2d, e). Consequently, an upshifted and a downshifted valence band emerge in the bilayer band diagram (black arrows Fig. 2e), causing a bandgap reduction. However, we observe that the upshifted band, which is the upmost valence band, is not involved in the main absorption peak. It plays instead an important role in the low-energy optical absorption.

The slowly decaying near-infrared absorption tail of PtSe₂ has been interpreted as originating from indirect interband absorption. We now provide the evidence that such a mechanism is not involved. Inspecting the computed optical absorption allows explaining the tail profile, only relying on direct optical transitions.

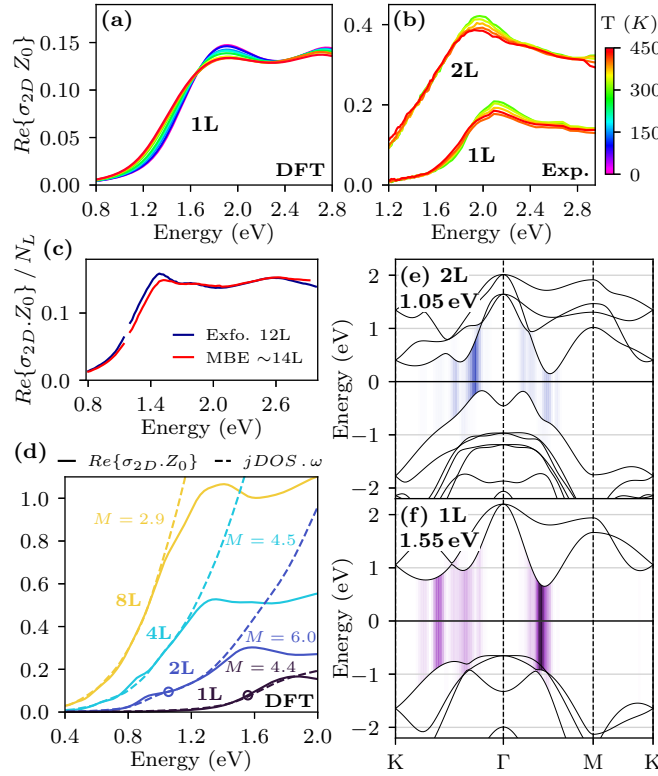


FIG. 3. Absorption tail origin. (a) Optical absorption $Re\{\sigma_{2D}\cdot Z_0\}$ of 1L for $T = 0 - 450$ K (computed) and of (b) 1L and 2L for $T = 290 - 440$ K (experimental). (c) Experimental real 2D optical conductivity of a 12L exfoliated flake and a ~ 14 L MBE-grown film [43], rescaled by the number of layers. (d) Computed $Re\{\sigma_{2D}\cdot Z_0\}$ (full line), and $jDOS\cdot\omega$ (dashed line, ω is the optical frequency) for 1L, 2L, 4L and 8L – rescaled by an *ad hoc* dipolar matrix coefficient M (expressed in Hartree atomic units). (e) 2L and (f) 1L contributions to the real 2D optical conductivity, at the energies circled in (d).

To this end, we investigate the role of phonons on the optical absorption [37] by using a temperature-dependent DFT simulation that treats simultaneously direct and phonon-assisted indirect processes [44, 45]. The absorption tail is mostly unaffected [46] by a 0 – 450 K temperature increase, indicating the dominance of direct transitions (Fig. 3a). This is confirmed experimentally by investigating 1L and 2L samples absorption while increasing the temperature from 290 to 440 K (Fig. 3b).

We also investigate the role of defects on optical absorption, by considering an exfoliated flake and a thin film grown by molecular beam epitaxy [43]. Both feature different Raman linewidths [29], testifying of different types and/or densities of defects [43, 47]. However, they present almost identical absorption tails (Fig. 3c).

Since indirect transitions are experimentally ruled out, we come back to the direct optical transition interpretation guided by the insights provided by DFT. We start by confronting the real part of the 2D optical conductivity σ_{2D} with the joint density of states $jDOS$ multiplied by frequency ω . As shown in Fig. 3d, they coincide over the absorption tail spectral range (~ 0.7 eV), so that we can write $Re\{\sigma_{2D}\} \sim M \cdot jDOS \cdot \omega$. This relation is expected for optical transitions featuring a constant light-matter coupling, that we identify here as M – suggesting that specific transitions, involving analogous pairs of states, are responsible for the tail absorption. We indeed identify these transitions by inspecting the contributions to optical absorption of 1L and 2L (Fig. 3e and f): they occur between the upmost p_z^+ -based valence band and a conduction band bearing Pt $d_{x^2-y^2/xy}$ orbital component. Due to band degeneracy lifting when stacking individual layers, the number of optical transitions involved in the absorption tail increases with the layers count. Consequently, the monolayer sample exhibits resonant transitions only 0.3 eV below its 1.85 eV peak, while the resonant transitions in 2L extend 0.7 eV below (Figs 3d, f). This explains the steeper absorption decrease of 1L (Fig. 1d bottom), which in turn leads to a stronger sensitivity to temperature-induced broadening (Fig. 3a, b).

While DFT is a tool providing valuable information about the coupling of electronic wavefunctions involved in optical transitions, its bandgaps estimates have limited accuracy. To illustrate this, we compare DFT-computed optical absorption using different DFT models (Fig. 4a), and observe a model-dependent energy shift of the absorption profiles. This is caused by different accounts of many-body interactions, which appear as a rigid shift of the conduction bands with respect to the valence ones (SM-5c) - a well-known limit of DFT methods [48]. This observation

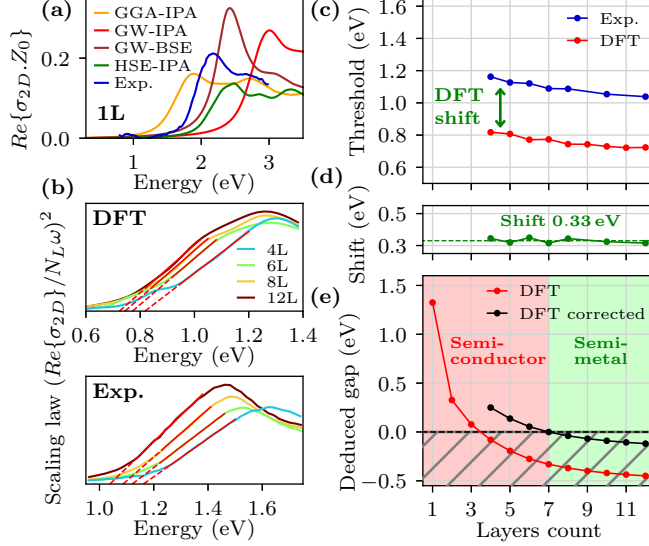


FIG. 4. DFT bandgap correction using the optical absorption tail. (a) Comparison of computed real 2D optical conductivities for monolayer PtSe₂ using several DFT methods. (b) Extraction of the tail threshold energy, for GGA DFT-computed and experimental absorptions, using linear extrapolation from the $(Re\{\sigma_{2D}\}/N_L\omega)^2$ scaling law (ω is the energy and N_L the layer count). (c) Experimental and theoretical threshold energies depending on the layers count, and (d) the inferred energy shift. (e) DFT-computed bandgap (red), and its value upshifted by 0.33 eV (black). The diagonal hatched area is the 0 eV gap region.

invites us to rescale the DFT calculations using the optical absorption measurements to determine the indirect bandgap energies and deduce the semiconductor-to-semimetal transition. More specifically, we use the NIR optical signature: the absorption tail. This latter has been used in previous works to extract PtSe₂ bandgaps using Tauc plots. We now rely on the knowledge that this tail results from direct transitions, and derive a scaling law for the bulk limit: close to the lowest energy direct transition ω_0 , the energy bands are locally quadratic in momentum and the light-matter coupling can be considered as constant, so that $(Re\{\sigma_{2D}\}/\omega)^2 \sim \omega - \omega_0$ (SM-5b). Applying this law to the GGA DFT-computed and experimental absorption tails, we extract threshold energies by extrapolating the linear slopes to the x-intercept, down to 4L thickness (Fig. 4b and c). Note that as the material is thinned down, 2D electronic confinement leads to the discretization of the z-momentum. Hence, the scaling law only applies for thick enough materials (in practice 4L). The inferred threshold values for experimental and simulated data feature a nearly constant 0.33 eV en-

ergy shift (Fig. 4d). We consequently upshift the DFT indirect bandgap predictions by this value (Fig. 4e). With this correction, the transition from indirect semiconductor to semimetal state occurs around 7 layers, in contrast with initial *ab initio* calculations which predicted PtSe₂ to be semiconducting up to 2-3 layers [10, 49]. Experimental electronic transport and scanning tunneling spectroscopy measurements reported transitions observed between 3 and 10 layers [9, 32–36]. These estimations present a large spread, which could be explained by the presence of spurious conduction channels due to defects or a lack of accuracy in the determination of the number of layers. In our work, by employing optical absorption spectroscopy we precisely establish the number of layers, and the use of an indirect method for determining the electronic bandgap makes it insensitive to the presence of defects. A 7-layer semiconductor-to-semimetal transition opens the possibility to fine-tune the electronic bandgap down to very low values – close to the transition, the bandgap shifts by only ~ 50 meV / layer – of particular interest for middle and far infrared optoelectronics.

The optical absorption mechanism demonstrated in our study is supported by robust sample-to-sample reproducibility. Mono and bilayers are however notable exceptions (Fig. 5a, d), which we further consider below.

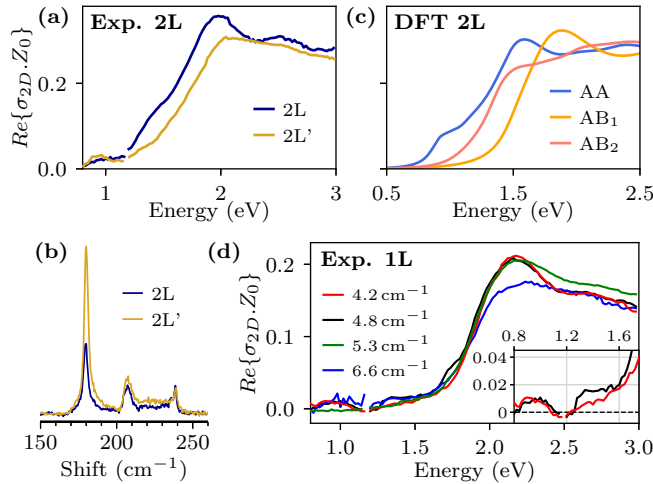


FIG. 5. Bilayer stacking and monolayer presumed bound exciton. (a) Experimental optical absorption of two bilayers, (b) featuring different Raman signatures. (c) DFT-computed optical absorption of 2L with AA, AB₁ or AB₂ stackings (structure in SM-4d). (d) Experimental monolayers optical absorption, labeled by their Raman E_g mode linewidth [29], and (inset) low-energy magnification.

The nature of the interlayer coupling strongly affects 2D materials optical absorption [50], and

in particular the one of bilayer PtSe₂. The Raman spectral signature allows to sort bilayers in two categories [29], labeled 2L and 2L' (Fig. 5b). With respect to 2L samples, the 2L' display a blue-shifted optical absorption, do not have an energy shoulder at 1.4 eV, and exhibit a low intensity absorption peak at 1.0 eV. These three features are shared with monolayer PtSe₂ (Fig. 5d), suggesting that the 2L' samples have a reduced interlayer coupling. If AA stacking (1T phase) is the most stable configuration of octahedral PtSe₂, AB stacking has been predicted to be stable as well [49, 51, 52] and has been found to be a common defect of grown films [43, 53, 54]. Comparing the simulated optical absorption of AA and of two types of AB stacking (Fig. 5c), we find that the AB stacked spectra present a characteristic blueshift, and do not display the 0.9 eV characteristic shoulder of the AA stacked spectrum. The optical absorption of 2L supports therefore an AA-stacked configuration, while the one of 2L' is likely caused by AB stacking.

We now turn to the PtSe₂ monolayers: the sample of worst crystalline quality, featuring a Raman E_g mode linewidth above 6 cm⁻¹ [29], presents a reduced 2.2 eV peak amplitude with respect to the best samples. This is not surprising as this peak results from band nesting effect, a singularity of the band structure that can be particularly altered by the presence of disorder – even more since it is affected by many-body interactions (GW-BSE in Fig. 4a).

Beyond redistribution of oscillator strength caused by many-body effects, one can wonder if bound excitons might be observed in PtSe₂. We have performed a photoluminescence experiment at room temperature within the visible range (SM-6). The measured signal is very weak, and no distinctive excitonic signatures can be identified. Inspecting the optical absorption of monolayer PtSe₂, an unexpected feature is nonetheless observed at lower energy: the high-quality samples, of Raman mode linewidth below 5 cm⁻¹, exhibit a 1 % absorption peak at 1.0 eV (Fig. 5d). This peak is located below the absorption tail, in the optical gap, and might well originate from a bound exciton. Future work is needed at low temperature to investigate further its origin.

In conclusion, we have shown that the NIR-vis optical absorption – peaks and low-energy tail – of indirect bandgap thin layered PtSe₂ arises from single-electron direct optical transitions. As a consequence, we could infer its semiconductor-to-semimetal transition at 7 layers. This direct and tunable optical absorption paves the way to efficient and ultrafast optoelectronics in the telecom band. Furthermore, the now available high-quality exfoliated PtSe₂ down to the monolayer allows exploring many-body effects, such as a potential monolayer exciton at 1.3 μm.

We thank Y. Chassagneux and F. Rapisarda for experimental help. The authors acknowledge the financial support from the European Union’s Horizon 2020 program under grant agreement no. 785219, no. 881603 (Core2 and 3 Graphene Flagship) and no. 964735 (FET-OPEN EXTREME-IR), as well as from ANR-2018-CE08-018-05 (BIRDS), ANR-2021-CE24-0025 (ELuSeM), ANR-20-CE09-0026 (2DonDemand), and Thales Systèmes Aéroportés (CIFRE grant No. 2016/1294). This work was granted access to the HPC resources of MesoPSL financed by the Region Ile de France and the project EquipMeso (reference ANR-10-EQPX-29-01) of the program Investissements d’Avenir supervised by the Agence Nationale pour la Recherche. Authors contributions are detailed in SM-7. Data are publicly available at [10.5281/zenodo.10138281](https://doi.org/10.5281/zenodo.10138281).

-
- [1] H. Schmidt, F. Giustiniano, and G. Eda, [Chemical Society Reviews](#) **44**, 7715 (2015).
 - [2] K. F. Mak and J. Shan, [Nature Photonics](#) **10**, 216 (2016).
 - [3] Y. Wang, L. Zhou, M. Zhong, Y. Liu, S. Xiao, and J. He, [Nano Research](#) **15**, 3675 (2022).
 - [4] R. L. Goff, M. Rosticher, Y. Peng, Z. Liu, T. Taniguchi, K. Watanabe, J.-M. Berroir, E. Bocquillon, G. Fève, C. Voisin, J. Chazelas, B. Plaçais, and E. Baudin, [2D Materials](#) **8**, 035035 (2021).
 - [5] Y. Wang, L. Li, W. Yao, S. Song, J. T. Sun, J. Pan, X. Ren, C. Li, E. Okunishi, Y.-Q. Wang, E. Wang, Y. Shao, *et al.*, [Nano Letters](#) **15**, 4013 (2015).
 - [6] G. Wang, Z. Wang, N. McEvoy, P. Fan, and W. J. Blau, [Advanced Materials](#) **33**, 2004070 (2021).
 - [7] F. Bonell, A. Marty, C. Vergnaud, V. Consonni, H. Okuno, A. Ouerghi, H. Boukari, and M. Jamet, [2D Materials](#) **9**, 015015 (2021).
 - [8] Y. Zhao, J. Qiao, Z. Yu, P. Yu, K. Xu, S. P. Lau, W. Zhou, Z. Liu, X. Wang, W. Ji, and Y. Chai, [Advanced Materials](#) **29**, 1604230 (2017).
 - [9] A. Ciarrocchi, A. Avsar, D. Ovchinnikov, and A. Kis, [Nature Communications](#) **9**, 919 (2018).
 - [10] R. A. B. Villaos, C. P. Crisostomo, Z.-Q. Huang, S.-M. Huang, A. A. B. Padama, M. A. Albao, H. Lin, and F.-C. Chuang, [npj 2D Materials and Applications](#) **3**, 2 (2019).
 - [11] F. Wang, G. Dukovic, L. E. Brus, and T. F. Heinz, [Science](#) **308**, 838 (2005).
 - [12] J. Xie, D. Zhang, X.-Q. Yan, M. Ren, X. Zhao, F. Liu, R. Sun, X. Li, Z. Li, S. Chen, Z.-B. Liu, and J.-G. Tian, [2D Materials](#) **6**, 035011 (2019).
 - [13] X. Chen, S. Zhang, L. Wang, Y.-F. Huang, H. Liu, J. Huang, N. Dong, W. Liu, I. M. Kislyakov,

- J. M. Nunzi, L. Zhang, and J. Wang, *Photon. Res.* **7**, 1416 (2019).
- [14] J. Shi, Y. Huan, M. Hong, R. Xu, P. Yang, Z. Zhang, X. Zou, and Y. Zhang, *ACS Nano* **13**, 8442 (2019).
- [15] X. Zhao, F. Liu, D. Liu, X.-Q. Yan, C. Huo, W. Hui, J. Xie, Q. Ye, C. Guo, Y. Yao, Z.-B. Liu, and J.-G. Tian, *Applied Physics Letters* **115**, 263102 (2019).
- [16] L. Wang, S. Zhang, N. McEvoy, Y.-y. Sun, J. Huang, Y. Xie, N. Dong, X. Zhang, I. M. Kislyakov, J.-M. Nunzi, L. Zhang, and J. Wang, *Laser & Photonics Reviews* **13**, 1900052 (2019).
- [17] D. P. Gulo, H. Yeh, W.-H. Chang, and H.-L. Liu, *Scientific Reports* **10**, 19003 (2020).
- [18] J. Fu, W. Xu, X. Chen, S. Zhang, W. Zhang, P. Suo, X. Lin, J. Wang, Z. Jin, W. Liu, and G. Ma, *The Journal of Physical Chemistry C* **124**, 10719 (2020).
- [19] G. A. Ermolaev, K. V. Voronin, M. K. Tatmyshevskiy, A. B. Mazitov, A. S. Slavich, D. I. Yakubovsky, A. P. Tselin, M. S. Mironov, R. I. Romanov, A. M. Markeev, I. A. Kruglov, S. M. Novikov, A. A. Vyshnevyy, A. V. Arsenin, and V. S. Volkov, *Nanomaterials* **11**, 3269 (2021).
- [20] C.-C. Chung, H. Yeh, P.-H. Wu, C.-C. Lin, C.-S. Li, T.-T. Yeh, Y. Chou, C.-Y. Wei, C.-Y. Wen, Y.-C. Chou, C.-W. Luo, C.-I. Wu, M.-Y. Li, L.-J. Li, W.-H. Chang, and C.-W. Chen, *ACS Nano* **15**, 4627 (2021).
- [21] Z. Zheng, Z. Peng, Z. Yu, H. Lan, S. Wang, M. Zhang, L. Li, H. Liang, and H. Su, *Results in Physics* **42**, 106012 (2022).
- [22] H. Su, Z. Zheng, Z. Yu, S. Feng, H. Lan, S. Wang, M. Zhang, L. Li, and H. Liang, *Nanomaterials* **13**, 795 (2023).
- [23] J. He, W. Jiang, X. Zhu, R. Zhang, J. Wang, M. Zhu, S. Wang, Y. Zheng, and L. Chen, *Phys. Chem. Chem. Phys.* **22**, 26383 (2020).
- [24] J. He, X. Zhu, W. Liu, E. Hu, J. Wang, and R. Zhang, *Nano Research* **15**, 6613 (2022).
- [25] S. Bae, S. Nah, D. Lee, M. Sajjad, N. Singh, K. M. Kang, S. Kim, G.-J. Kim, J. Kim, H. Baik, K. Lee, and S. Sim, *Small* **17**, 2103400 (2021).
- [26] S. B. Desai, S. R. Madhvapathy, M. Amani, D. Kiriya, M. Hettick, M. Tosun, Y. Zhou, M. Dubey, J. W. Ager III, D. Chrzan, and A. Javey, *Advanced Materials* **28**, 4053 (2016).
- [27] M. Heyl, D. Burmeister, T. Schultz, S. Pallasch, G. Ligorio, N. Koch, and E. J. W. List-Kratochvil, *physica status solidi (RRL) – Rapid Research Letters* **14**, 2000408 (2020).
- [28] M. O'Brien, N. McEvoy, C. Motta, J.-Y. Zheng, N. C. Berner, J. Kotakoski, K. Elibol, T. J. Pen-

- nycook, J. C. Meyer, C. Yim, M. Abid, T. Hallam, J. F. Donegan, S. Sanvito, and G. S. Duesberg, [2D Materials](#) **3**, 021004 (2016).
- [29] M. Tharrault, E. Desgué, D. Carisetti, B. Plaçais, C. Voisin, P. Legagneux, and E. Baudin, [2D Materials](#) **11**, 025011 (2024).
- [30] Y. Li and T. F. Heinz, [2D Materials](#) **5**, 025021 (2018).
- [31] W. Zhao, Z. Ghorannevis, L. Chu, M. Toh, C. Kloc, P.-H. Tan, and G. Eda, [ACS Nano](#) **7**, 791 (2013).
- [32] C. Yim, V. Passi, M. C. Lemme, G. S. Duesberg, C. Ó Coileáin, E. Pallecchi, D. Fadil, and N. McEvoy, [npj 2D Materials and Applications](#) **2**, 5 (2018).
- [33] L. Ansari, S. Monaghan, N. McEvoy, C. Ó. Coileáin, C. P. Cullen, J. Lin, R. Siris, T. Stimpel-Lindner, K. F. Burke, G. Mirabelli, R. Duffy, E. Caruso, R. E. Nagle, G. S. Duesberg, P. K. Hurley, and F. Gity, [npj 2D Materials and Applications](#) **3**, 33 (2019).
- [34] T. Das, E. Yang, J. E. Seo, J. H. Kim, E. Park, M. Kim, D. Seo, J. Y. Kwak, and J. Chang, [ACS Applied Materials & Interfaces](#) **13**, 1861 (2021).
- [35] L. Zhang, T. Yang, M. F. Sahdan, Arramel, W. Xu, K. Xing, Y. P. Feng, W. Zhang, Z. Wang, and A. T. S. Wee, [Advanced Electronic Materials](#) **7**, 2100559 (2021).
- [36] J. Li, S. Kolekar, M. Ghorbani-Asl, T. Lehnert, J. Biskupek, U. Kaiser, A. V. Krasheninnikov, and M. Batzill, [ACS Nano](#) **15**, 13249 (2021).
- [37] P. Y. Yu and M. Cardona, Optical properties i, in *Fundamentals of Semiconductors: Physics and Materials Properties* (Springer Berlin Heidelberg, Berlin, Heidelberg, 2010) pp. 243–344.
- [38] J. Ji, Y. Zhou, B. Zhou, E. Desgué, P. Legagneux, P. U. Jepsen, and P. Bøggild, [ACS Applied Materials & Interfaces](#) **15**, 51319 (2023).
- [39] M. Hemmat, S. Ayari, S. Dhillon, *et al.*, Article in preparation (2023).
- [40] B. D. Viezbicke, S. Patel, B. E. Davis, and D. P. Birnie III, [physica status solidi \(b\)](#) **252**, 1700 (2015).
- [41] W. C. Dash and R. Newman, [Phys. Rev.](#) **99**, 1151 (1955).
- [42] A. Carvalho, R. M. Ribeiro, and A. H. Castro Neto, [Phys. Rev. B](#) **88**, 115205 (2013).
- [43] E. Desgué, P. Legagneux, *et al.*, Article in preparation (2023).
- [44] M. Zacharias and F. Giustino, [Phys. Rev. B](#) **94**, 075125 (2016).
- [45] M. Zacharias and F. Giustino, [Phys. Rev. Res.](#) **2**, 013357 (2020).
- [46] A small energy shift is due to electronic band structure renormalization with temperature (see SM-4civ).

- [47] P. Maguire, D. S. Fox, Y. Zhou, Q. Wang, M. O'Brien, J. Jadwiszczak, C. P. Cullen, J. McManus, S. Bateman, N. McEvoy, G. S. Duesberg, and H. Zhang, [Phys. Rev. B **98**, 134109 \(2018\)](#).
- [48] F. Hüser, T. Olsen, and K. S. Thygesen, [Phys. Rev. B **87**, 235132 \(2013\)](#).
- [49] A. Kandemir, B. Akbali, Z. Kahraman, S. V. Badalov, M. Ozcan, F. Iyikanat, and H. Sahin, [Semiconductor Science and Technology **33**, 085002 \(2018\)](#).
- [50] J. Liang, D. Yang, J. Wu, J. I. Dadap, K. Watanabe, T. Taniguchi, and Z. Ye, [Phys. Rev. X **12**, 041005 \(2022\)](#).
- [51] L. Fang, W. Liang, Q. Feng, and S.-N. Luo, [Journal of Physics: Condensed Matter **31**, 455001 \(2019\)](#).
- [52] R. Kempt, S. Lukas, O. Hartwig, M. Prechtel, A. Kuc, T. Brumme, S. Li, D. Neumaier, M. C. Lemme, G. S. Duesberg, and T. Heine, [Advanced Science **9**, 2201272 \(2022\)](#).
- [53] L. Xu, H. Liu, C. Song, X. Li, F. Li, D. Li, L. Wang, X. Bai, and J. Qi, [2D Materials **8**, 025014 \(2021\)](#).
- [54] G. H. Ryu, J. Chen, Y. Wen, and J. H. Warner, [Chemistry of Materials **31**, 9895 \(2019\)](#).

The optical absorption in indirect semiconductor to semimetal PtSe₂ arises from direct transitions - Supplemental Material

Marin Tharrault,¹ Sabrine Ayari,¹ Mehdi Arfaoui,² Eva Desgué,³ Romaric Le Goff,¹ Pascal Morfin,¹ José Palomo,¹ Michael Rosticher,¹ Sihem Jaziri,^{2,4} Bernard Plaçais,¹ Pierre Legagneux,³ Francesca Carosella,¹ Christophe Voisin,¹ Robson Ferreira,¹ and Emmanuel Baudin^{1,5}

¹*Laboratoire de Physique de l'Ecole normale supérieure, ENS, Université PSL, CNRS, Sorbonne Université, Université de Paris, 24 rue Lhomond, 75005 Paris, France*

²*Laboratoire de Physique de la Matière Condensée, Faculté des Sciences de Tunis, Université Tunis El Manar, Campus Universitaire 1060 Tunis, Tunisia.*

³*Thales Research & Technology, 91767 Palaiseau, France*

⁴*Laboratoire de Physique des Matériaux : Structure et Propriétés, Faculté des Sciences de Bizerte, Université de Carthage, 7021 Jarzouna, Tunisia.*

⁵*Institut universitaire de France*

CONTENTS

1. Au-assisted mechanical exfoliation	3
2. Atomic force microscopy - thickness determination	4
3. Micro-absorption spectroscopy	4
a. Working principle	4
b. Corrections and performances	7
i. Focus corrections and spatial resolution	7
ii. Finite numerical aperture effects	8
iii. Aberrations correction and accuracy	9
c. Optical conductivity calculation	10
d. Temperature-dependent differential reflection	12
e. Monolayer 1.0 eV peak	12
4. Simulation of the optical absorption	13
a. Density functional theory of the 1L to 12L band structure	13
b. Optical conductivity computation	15
i. Simulation and formula	15
ii. Contributions diagram	16
c. Further corrections applied to monolayer PtSe ₂	17
i. From GGA functional to GW	18
ii. Bethe-Salpeter Equation correction	19
iii. Hybrid functional HSE06	19
iv. Finite temperature optical absorption	21
d. AB stacked bilayers	23
e. Orbital projected partial density of states	24
i. Simulation method	24
ii. Orbitals projections	24
iii. Orbitals decomposition of optical transitions	25
5. Density of states, peaks and low-energy scaling	27
a. Optical absorption and jDOS	27

b. Low-energy scaling law	28
c. Rigid shift hypothesis	30
6. Photoluminescence of exfoliated flakes	31
7. Authors contributions	32
References	32

1. AU-ASSISTED MECHANICAL EXFOLIATION

The process used to mechanically exfoliate few-layers PtSe₂ flakes is adapted from the one developed by Desdai *et al.* [1], and is schematized in Fig. 1. A first coarse exfoliation of a bulk crystal grown by CVT (HQ graphene) is performed with standard blue tape onto a clean SiO₂/Si substrate. The sample is cleaned in acetone/IPA and a 60 nm Au layer is deposited by Joule evaporation. It is followed by a 150°C anneal in order to create differential dilation between Au and the PtSe₂ stack [2] thereby detaching few layers of crystal. Finally the Au layer is peeled off using thermal release tape and freed on a fused silica substrate, alongside with few layers PtSe₂ flakes. The glue residues on the top layer of Au are removed using acetone/IPA from and the Au is etched with a solution of KI₂ (4 KI : 1 I₂ : 400 H₂O, about 100 – 200 nm/min).

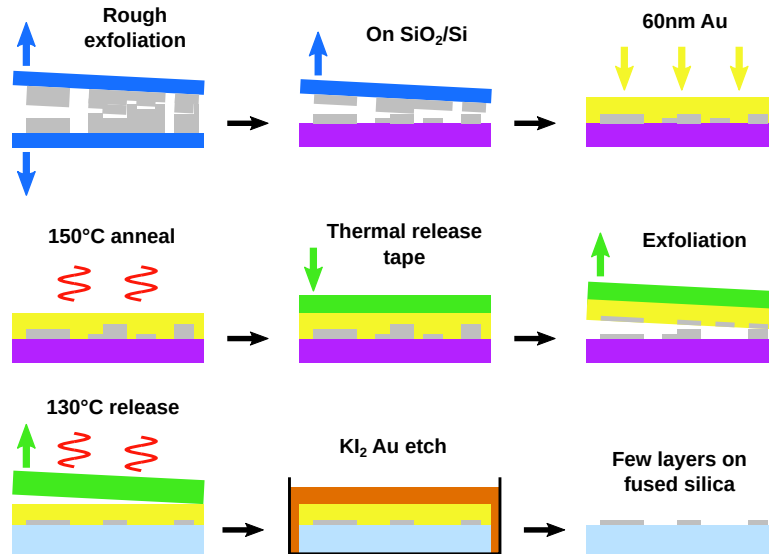


FIG. 1. Au-assisted exfoliation protocol.

The narrow Raman spectral peaks recorded, compared to those originating from PtSe₂ films

obtained with CVD, MBE or mechanical exfoliation in other works [3], is an assessment of the structural quality of the obtained flakes, apparently unperturbed by the Au-assisted exfoliation technique.

2. ATOMIC FORCE MICROSCOPY - THICKNESS DETERMINATION

Identification of the layer number of the exfoliated flakes is not obvious on such a new material as PtSe₂. The absorption in the green-blue range 2.5 – 3.0 eV appears to be the best means for such a characterization, since it evolves linearly with the flake thickness. In order to provide consistent proof of it, the deduced thickness has been crossed-checked with Atomic Force Measurement (AFM), using a Dimension Edge Bruker system.

It is well known that measuring a flake to substrate step height is not a reliable method to determine the flake’s absolute number of layers: an interface layer of water is often present in between the flake and the substrate, which can reach ~ 1 nm. Yet, the step height between flakes of different thicknesses reliably establishes their layer count difference. As depicted in Fig. 2, the layer count identified with absorption spectroscopy is in agreement with the measured step heights. The individual layer thickness deduced from these measurements is 0.5 nm, in agreement with the one computed by DFT (section 4a) and measured by x-ray diffraction by the crystal supplier on PtSe₂ powder [4].

Raman spectroscopy is used as a complementary tool to identify between the flakes the ones of identical signature – and therefore identical number of layers – e.g., to assess that the bilayers of top and bottom rows in Fig. 2 are of identical thicknesses.

3. MICRO-ABSORPTION SPECTROSCOPY

In this section we present the operational functioning and details of the micro-absorption experiment.

a. Working principle

Polychromatic light (400 – 2200 nm) is produced by a supercontinuum laser, filtered to avoid second order diffraction on the spectrometers gratings, and mode-cleaned using an endlessly single-mode fiber, as depicted on Fig. 3. This light is focused with high numerical aperture apochromatic

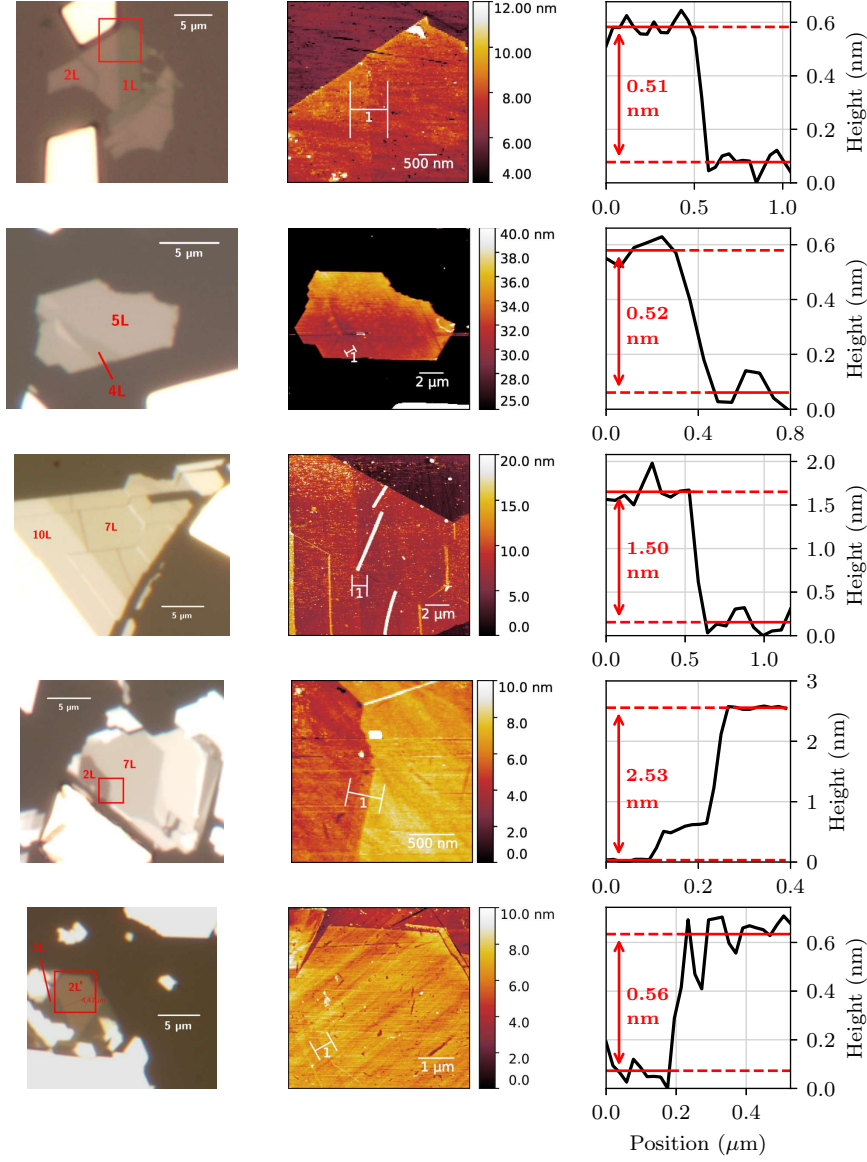


FIG. 2. PtSe₂ flakes AFM step heights. 1st column: pictures of PtSe₂ flakes, each area labeled with its layers count. When needed, the area studied is indicated as a red square. Very bright areas are gold pads used to normalize the reflection, these pads are not present in the AFM scan. 2nd column: AFM height mappings. Cuts are indicated with "1" labels. 3rd column: Height profiles along the cut. Using a layer thickness of 0.5 nm, we deduce a step height of 1, 1, 3 and 5 layers from top to bottom flakes, in agreement with the optical absorption identification.

microscope objectives (one for the visible, one for the NIR) onto the sample (typical power 30 μ W over a bandwidth of 300 nm). The sample position is scanned using 3-axes piezoelectric positioners. Reflected and transmitted light as well as a power reference are collected by multimode fibers and

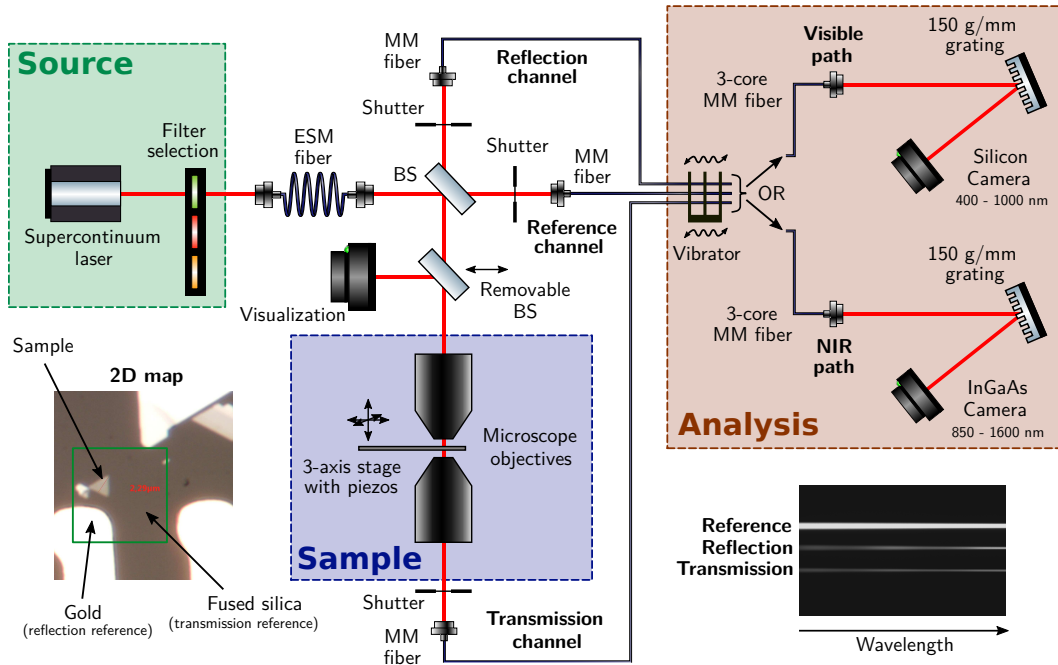


FIG. 3. Schematic of the micro-absorption experiment. **Source**: polychromatic light is emitted by a super-continuum laser and transmitted using achromatic optical elements. **Sample**: a pair of microscope objectives focus the light on the sample and collect its reflection and transmission. **Analysis**: spectrometers in the visible or in the infra-red record reflection, transmission and reference channels spectra. 2D mappings allow measuring a specific flake in addition to the highly reflective gold and transmissive fused silica reference.

transmitted to visible or NIR spectrometers. The fibers are coiled around a vibrating device to time-average spurious speckles, and then combined into a 3-core multi-mode fiber. The output light from the fiber is focused on the input slit of the spectrometer. Gratings of 150 g/mm are used, enabling nanometric resolution as well as a large spectral range. The full visible / NIR spectra are reconstituted by combining several acquisitions. Such spectra are collected while 2D mappings are performed, including the region of interest and absolute references for the reflection and transmission: highly reflective evaporated 120 nm gold surfaces and the transmissive fused silica substrate, used to normalize *in situ* the reflection and the transmission respectively (reference data from [5, 6]).

The supercontinuum laser presents a rather flat spectral power density, at the notable exception of the wavelengths close to its pump power at 1064 nm where it is an order of magnitude larger. We therefore use a notch filter to suppress this spectral range, which appears in the data as a gap,

located at 1.2 eV (main text Fig. 1d).

b. Corrections and performances

i. Focus corrections and spatial resolution

While capturing 2D mappings, a focus plane is used to take into account small sample misorientation. Microscope objectives focal shifts are as well corrected on the full visible to NIR range. Additionally, a refocusing system is periodically scanning for the optimal focus to compensate long-term thermal shifts.

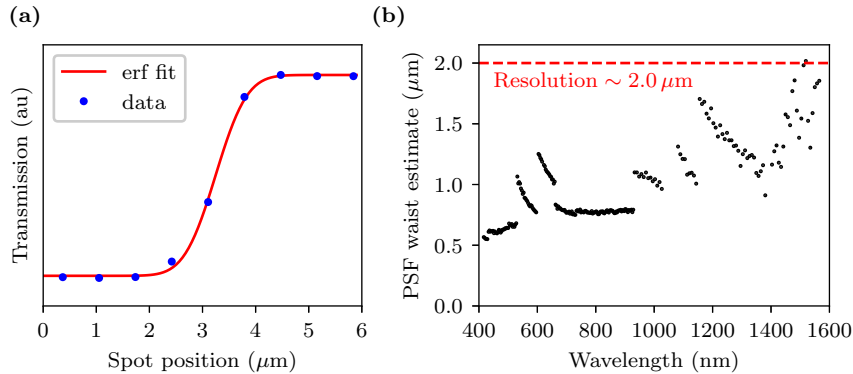


FIG. 4. Spatial resolution measured with the knife-edge method. (a) Transmitted light while moving the spot from an exfoliated flake to the substrate. The data points are fitted with an error function, modeling the convolution of the PSF with a step-function. (b) Spectral point spread function (PSF) waist estimate from the fit, taken as twice the Gaussian standard deviation. Its maximum value provides the setup spatial resolution, that is about of $2.0 \mu\text{m}$. The discontinuous nature of the plot is originating from the adjustment of the microscope objective focus while changing of wavelength range. The data used for the knife-edge method originate from a typical hyperspectral mapping.

Adding to these precautions a careful alignment of the microscope objective leads to a micrometric spatial resolution over the whole spectral range. The spatial resolution can be measured using the knife edge method Fig. 4, giving a value of $2.0 \mu\text{m}$.

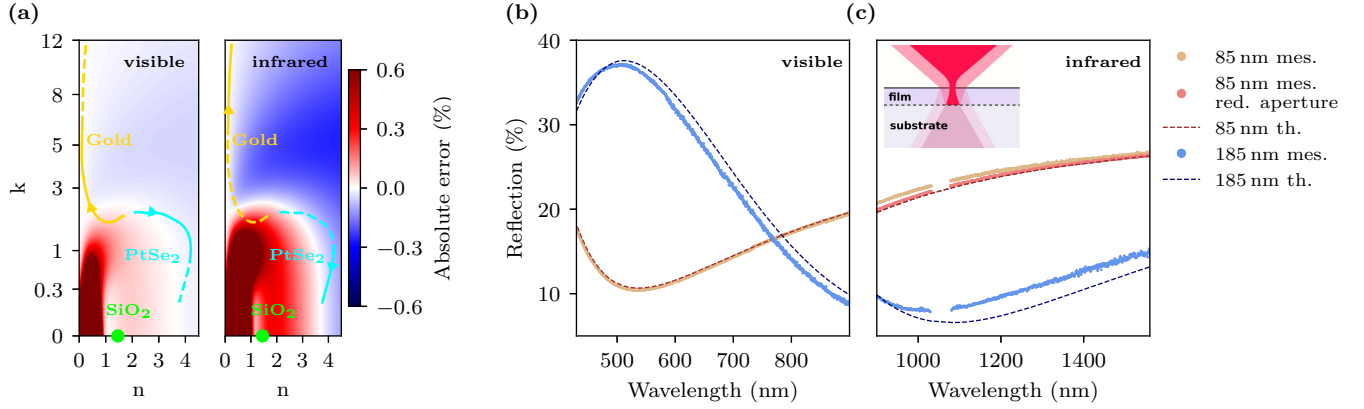


FIG. 5. Finite numerical aperture (NA) effects on the measurement accuracy. (a) Computation of the absolute error made on the reflection by neglecting finite numerical aperture effects, as a function of the real and imaginary parts of the substrate’s refractive index $n + ik$. It is displayed as a colormaps for the objectives used in the visible (NA = 0.5, left) and in the NIR (NA = 0.7, right). The green dots, solid yellow and blue lines display the refractive indices of SiO₂, gold and PtSe₂ respectively, the arrow pointing towards increasing wavelengths. The error on the transmission at the interface is the opposite of the error on the reflection pictured in panel (a). (b) Measured (dotted lines) and computed (dashed lines) reflection for an 85 nm (brown) and 185 nm (blue) thick SiO₂ layer on top of a Si substrate, on the visible range. (c) Same measurement performed on the NIR range. The red dots are measured on 85 nm SiO₂/Si while reducing the microscope objective aperture by a factor of 2. (inset) Scheme picturing the internal reflections in the SiO₂ slab. The SiO₂/Si stepwafer has been calibrated by ellipsometry. The Refractive indexes for the SiO₂, gold, PtSe₂ and Si are extracted from [5–8].

ii. Finite numerical aperture effects

In this section, we investigate errors that may arise when using a focused light beam in our experiment. The thin film model utilized to retrieve intrinsic optical properties assumes that the incoming beam is at normal incidence with respect to the surface. Neglecting these errors may not seem obvious considering the high numerical apertures of the microscope objectives. We estimate consequently the error made on the reflection or transmission of PtSe₂, gold or fused silica interface (by modelling a uniform illumination of the microscope aperture). We study separately visible and NIR ranges (which rely on different microscope objectives), and display the estimates using color maps (Fig. 5a). We find an error that reaches in absolute value at most 0.3%, which is below the setup accuracy.

We moreover impose that the reflections interfering within the film perfectly overlap with each other – as opposed to a situation where a thicker film would have internal reflections whose spot diameters present increasing diameters, as pictured in the inset of Fig. 5c. This condition enables exact modelling of the interference phenomenon and eventually permits precise determination of the optical indices. To quantify this phenomenon, we compare the reflection measured from an ellipsometry calibrated SiO₂/Si step-wafer with its theoretically expected value. In the visible – using the appropriate microscope objective – the measured reflectance features a shift compared to the predicted one for an 185 nm thick SiO₂ layer while it shows good agreement for an 85 nm thick SiO₂ layer (Fig. 5b). The effect is more pronounced in the infrared, since both stepwafers reflections present a shift with the expected values – because of the higher numerical aperture of the objective. This effect can be however suppressed by reducing the objective aperture diameter, enabling to recover a fair agreement between measured and predicted values. Accurate measurements of reflection (or transmission) therefore require the film under study to be sufficiently thin, typically below $e_{\text{SiO}_2} \sim 40$ nm which translates in terms of PtSe₂ thickness as:

$$e_{\text{PtSe}_2} < \frac{\delta}{n_{\text{PtSe}_2}} \sim \frac{n_{\text{SiO}_2}}{n_{\text{PtSe}_2}} e_{\text{SiO}_2} \sim 15 \text{ nm} \quad (1)$$

In this work we study at most 12L of PtSe₂, which represents a thickness of about 6 nm.

iii. Aberrations correction and accuracy

The roughness of the 150 g/mm grating of the visible spectrometer is responsible for light scattering out of the first diffraction order. This aberration is tackled by independent channel acquisitions and background fitting. The Silicon and InGaAs cameras are moreover carefully operated in their linearity ranges. Under these conditions, the acquired spectra feature a typical 0.5% accuracy as it can be inferred from the SiO₂/Si step-wafer reflection measurement (for 85 nm SiO₂ in the visible range and 185 nm SiO₂ with a reduced aperture in the NIR range, Fig. 5b and c).

However the use of the gold metallic surface as a reflection reference is only applicable beyond the 500 nm gold 5d to 6s transition. Indeed this resonance enables the existence of plasmonic modes, which are strongly sensitive to the surface roughness, and in turn, impact the reflectivity [5, 9]. In order to correctly normalize data in this range, we rather use the fused silica as a reference for reflection. It is however poorly reflective, with a typical 4% reflectance, and systematic errors made on this value (as in Fig. 5a) are amplified while normalizing for the resulting reflectance. To solve

this issue, we offset the data on the 400 – 600 nm range where fused silica is used as reference to match the one on the > 600 nm range where the reference is the gold surface (this offset reaches typically 0.5 %).

c. Optical conductivity calculation

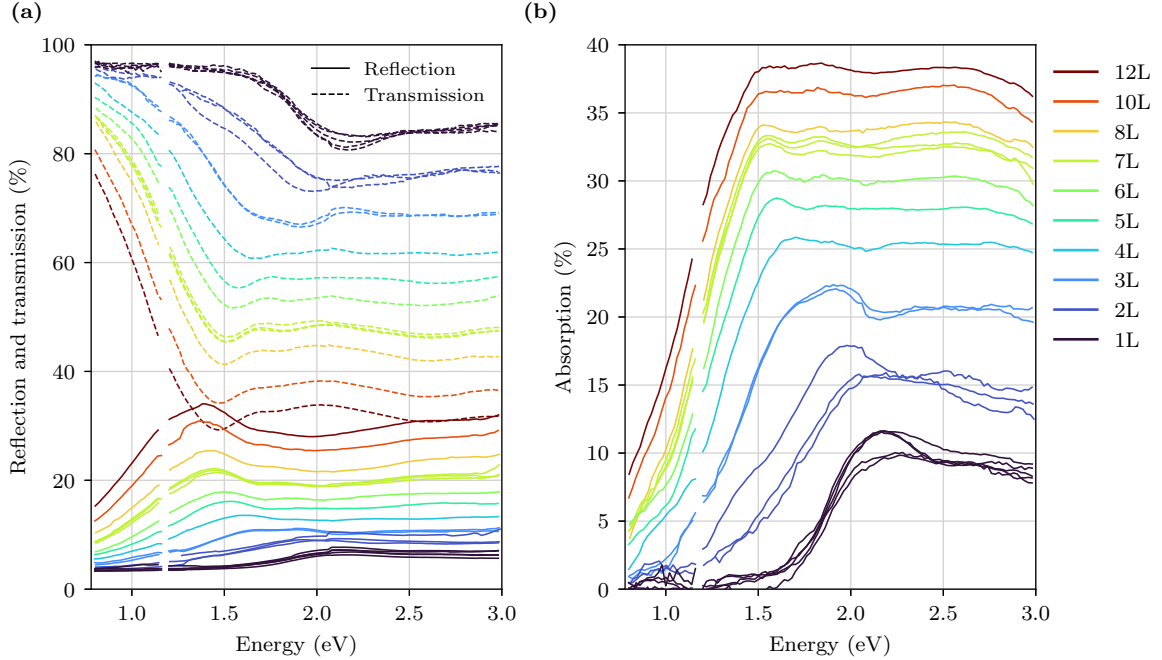


FIG. 6. Absolute optical spectra of PtSe₂ flakes on a fused silica substrate. (a) Reflection, transmission and (b) absorption channels.

From the spectral data of absolute reflection R and transmission T (Fig. 6), we can infer the 2D complex optical conductivity σ_{2D} of the films by modelling their reflection and transmission at the air / substrate interface [10]:

$$R = \left| \frac{1 - n_S - Z_0 \sigma_{2D}}{1 + n_S + Z_0 \sigma_{2D}} \right|^2 ; \quad T = \text{Re}\{n_S\} \left| \frac{2}{1 + n_S + Z_0 \sigma_{2D}} \right|^2 \quad (2)$$

where n_S is the substrate optical index and $Z_0 = 377 \Omega$ is the impedance of the vacuum. The resulting spectra for 1 to 12 layers are displayed in Fig. 7, binned using a 20 meV span.

As detailed by Li and Heinz [10], the differential reflection, differential transmission and absorption scale – up to a constant factor – with the real part of the optical conductivity $\text{Re}\{\sigma_{2D}\}$ (for a dielectric substrate and a film sufficiently thin). Therefore, the method we use derives unambiguously the real part of the optical conductivity $\text{Re}\{\sigma_{2D}\}$. It also allows to derive the imaginary

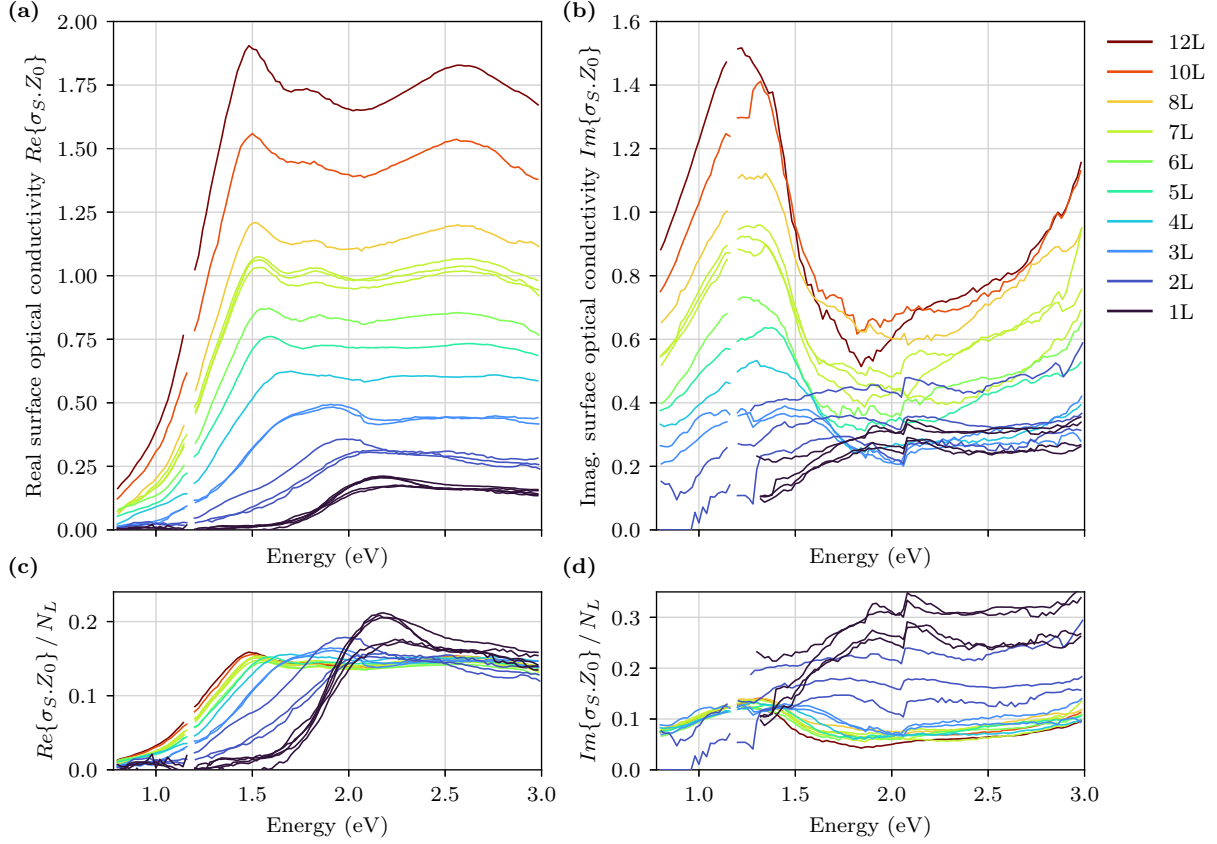


FIG. 7. Measured 2D optical conductivity. (a) Real, and (b) imaginary parts of the optical conductivity, and their respective values divided by the number of layers (c and d). Data of $Im\{\sigma_{2D}\}$ is discarded for 1L low absorption values.

part of the optical conductivity $Im\{\sigma_{2D}\}$, but for a non-vanishing optical absorption. On the other side, when using DFT, $Im\{\sigma_{2D}^{th}\}$ is inferred by Kramers-Kronig inversion of $Re\{\sigma_{2D}^{th}\}$ (which involves a long-range integral), and is therefore very sensitive to oscillator strength misestimations. Consequently the data of $Im\{\sigma_{2D}\}$ are not commented in our work.

The complex optical conductivity is the adequate quantity to quantify a thin film optical response, as the resulting quantity is independent of the slab thickness. Considering the complex optical conductivity instead of the bulk dielectric permittivity is permitted under the assumption of a negligible phase shift in the thin slab. This can be done under the condition $|Z_0\sigma_{2D}| \ll |n|$ [10]. In our case, $|n_{PtSe_2}| \sim 4$ (Fig. 5a), while $|Z_0\sigma_{2D}|$ reaches at most 2 for 12L stacking. This condition is therefore not strictly respected for the thick flakes. However, the excellent agreement between the normalized real conductivities of 10L and 12L (Fig. 7c) gives confidence in the fair accuracy of the procedure.

d. Temperature-dependent differential reflection

In order to vary the sample's temperature, we adapt the sample holder to include a planar resistive heater. The temperature can be varied between 290 K and 440 K, and the presence of the heater allows only the reflection channel to be collected, not the transmission channel. Differential reflectance spectra $\Delta R/R = (R_{\text{sample}} - R_{\text{substrate}}) / R_{\text{substrate}}$ are acquired and displayed in Fig. 8.

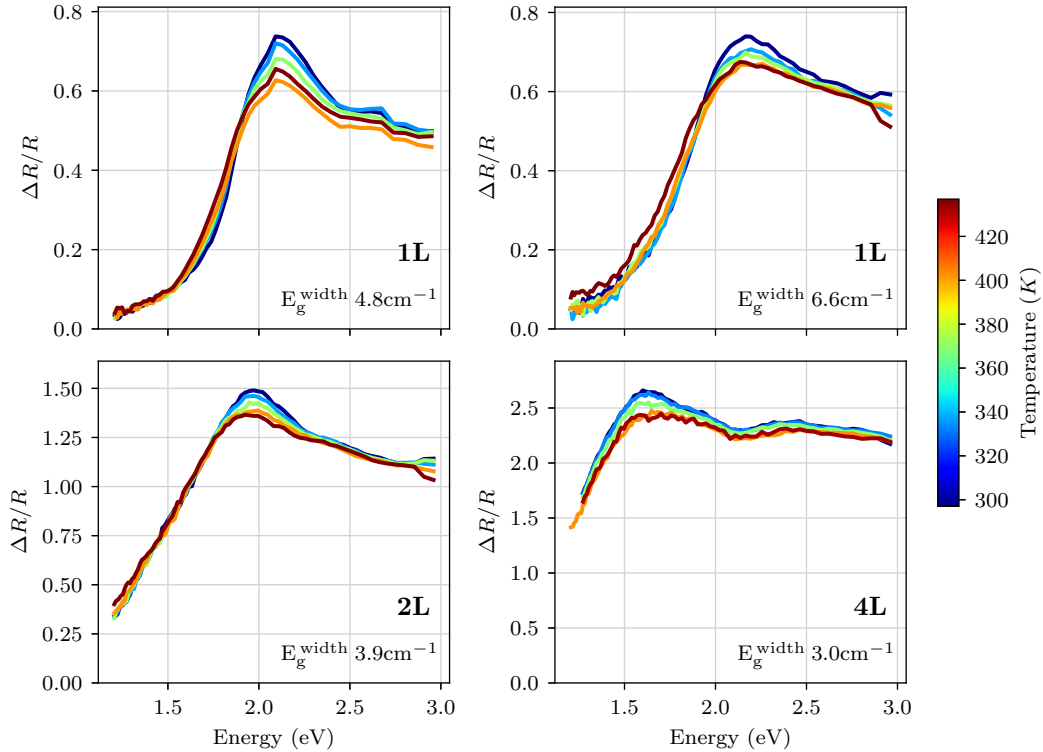


FIG. 8. Differential reflectance of 1L, 2L and 4L flakes, featuring various samples quality characterized by the Raman E_g mode linewidth [3]. Temperature is varied in the range 290 – 440 K. Although the two monolayer samples feature different qualities, their temperature dependencies appear to be similar.

One can relate the differential reflectance with the real 2D optical conductivity, as detailed in [10], under the assumption of very low optical thickness $|Z_0\sigma^s| \ll 1$. This is what is used to compute the real optical conductivity for 1L and 2L PtSe₂ in main text Fig. 3a.

e. Monolayer 1.0 eV peak

Monolayer PtSe₂ features a small peak at 1.0 eV (Fig. 9a) for the highest quality samples – the ones featuring the lowest E_g Raman mode linewidth [3], of 4.2 and 4.8 cm^{-1} . One could suspect such

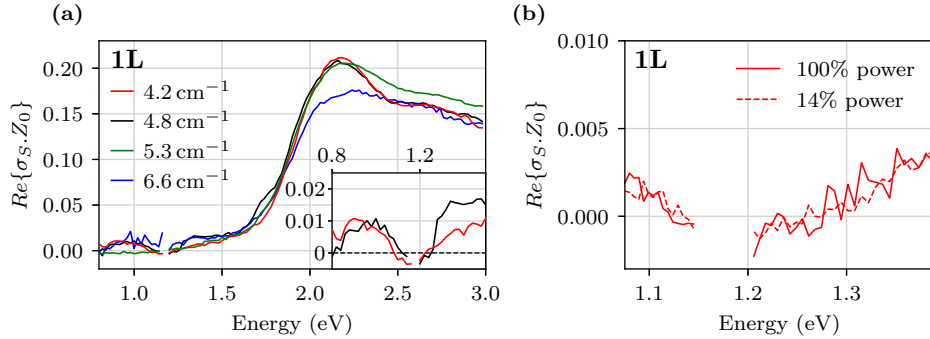


FIG. 9. Monolayer PtSe₂ low energy absorption peak. (a) 1L real 2D optical conductivity, labeled by the Raman E_g mode linewidth [3]. (b) The same quantity on a more restricted range, for the highest-quality sample (4.2 cm^{-1}), with the laser operating at full power (full line), and at 14 % (dashed line).

peak to originate from the nature of the supercontinuum laser, which is based on a strong pulsed pump at 1.19 eV (1064 nm). However reducing the laser power to 14 % of its maximum setting does not modify the optical absorption close to this wavelength, ruling out the possibility for this 1.0 eV peak to be an artifact.

4. SIMULATION OF THE OPTICAL ABSORPTION

a. Density functional theory of the 1L to 12L band structure

Structural relaxation, electronic band structure and density of states computations are performed within the Density Functional Theory (DFT) formalism by using the Quantum Espresso (QE) package, which is an integrated suite of open-source codes for the electronic structure calculation and materials modeling at the nanoscale [11–13]. The result of DFT calculations depends on the choice of exchange-correlation functional (LDA, GGA, meta-GGA, etc.). This choice is done according to the specificities of the system under study, and more complex functionals are more computation-intensive, calling for a trade-off between accuracy and computational speed. In our DFT calculation, the norm-conserving pseudo-potential with the Perdew-Burke-Ernzerhof (PBE) version of the generalized gradient approximation (GGA) is used to treat the exchange correlation interactions between valence electrons [14, 15]. Since PtSe₂ has a layered structure, the van der Waals (vdW) force between different layers are taken into account by first-principles calculations for a better accuracy [16–19]. In our work, a vdW correction of the PBE functional is therefore performed using Tkatchenko-Scheffler (TS) method [19]. The initial lattice constant for bulk 1T – PtSe₂ is taken

from the materials project website [20], and is optimized for the chosen pseudo-potential, by using the quasi-Newton schemes as implemented in the QE package [21]. The optimized lattice constants of the 1T bulk are then used as initial parameters for the layered structures from 1L up to 12L and then relaxed. As DFT relies on periodic boundary conditions, a vacuum space of at least 15 Å between periodic images of the structure along the [001] direction is used in order to avoid spurious couplings. The cutoff energy and \mathbf{k} -point sampling were tested with a PBE-GGA calculation in a convergence study to ensure numerical stability. The kinetic energy cutoff for a plane-wave basis set was taken as 680 eV. An appropriate Monkhorst-Pack \mathbf{k} -point sampling [22] of the Brillouin zone is used, centered with $15 \times 15 \times 1$, $20 \times 20 \times 1$, and $40 \times 40 \times 1$ meshes (for structure, self-consistent calculation, and projected density of states, respectively). The convergence criterion of self-consistent calculations for electronic structure and ionic relaxations is to reach a 10^{-8} eV difference between two consecutive steps. During the optimization process, all atoms were free to move in all directions of space to minimize the internal forces down to 10^{-5} Rydbergs per Bohr radius.

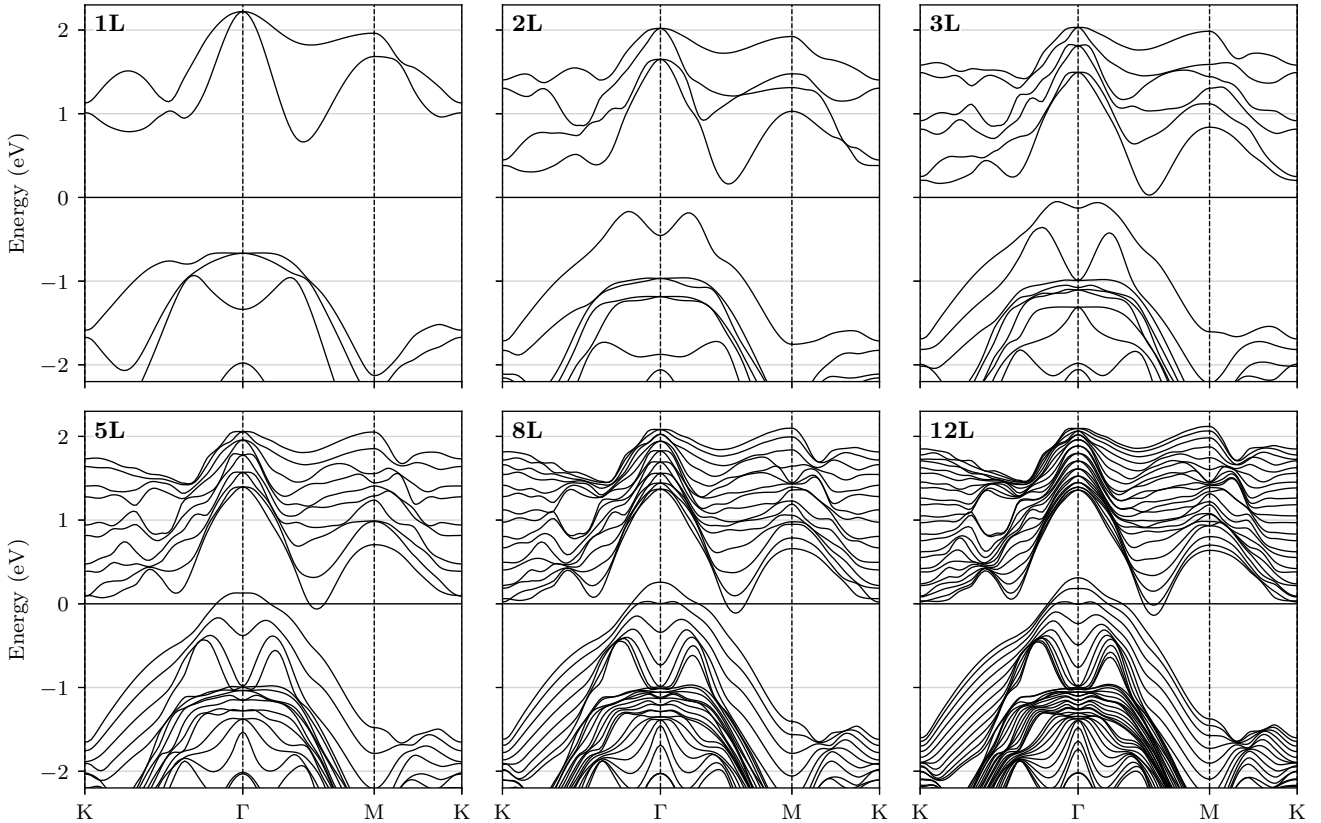


FIG. 10. Band diagrams computed with GGA-PBE approximation for 1, 2, 3, 5, 8 and 12 layers 1T – PtSe₂.

The 1T polytype of PtSe₂ crystallizes in the centrosymmetric *CdI2*-type structure with space

group $P\bar{3}m1$ and point group $D_{3d}(-3m)$ [23, 24]. The structure can be regarded as hexagonal closely packed Se atoms with Pt atoms occupying the octahedral sites in alternate Se layers. The adjacent Se layers are held together by weak van der Waals interactions [25]. The optimised lattice constant of the primitive unit cell of the monolayer 1T – PtSe₂ structure is found to be 3.72 Å. Atomic positions in the monolayer form do not deviate appreciably from the bulk – featuring a lattice constant of 3.78 Å – indicative of strong bonding between the Pt and Se atoms. Lattice constants are detailed in table 4a and are in agreement with previous works [26–28]. The mean Pt – Pt spacing is comparable with the single layer spacing measured by AFM on the exfoliated crystals (section 2)

	1L	2L	3L	5L	8L	12L
a (Å)	3.72	3.74	3.75	3.76	3.77	3.78
$\langle d_{Pt-Pt} \rangle$ (Å)	-	5.17	5.13	5.11	5.10	5.08

TABLE I. Optimized lattice parameter a , and average Pt-Pt distance d_{Pt-Pt} for each layer count.

b. Optical conductivity computation

i. Simulation and formula

After obtaining the DFT-Kohn Sham (KS) eigensystem using QE, we use the Yambo code [29–31], to compute the direct interband dipolar matrix elements, involved in the linear optical response. They take the form $\langle m, \mathbf{k} | \hat{r}_\alpha | n, \mathbf{k} \rangle$, with $|n, \mathbf{k}\rangle$ the single particle Bloch function of the n -th band obtained by DFT-KS computation for the wavevector \mathbf{k} , and \hat{r}_α the position operator along the α direction. These matrix elements contain all the symmetries imposed by the selection rules. For this computation, a plane-wave basis set is employed with a cutoff energy of 680 eV, and a total of 50 bands are included to ensure convergence of all computed quantities.

We consequently compute the diagonal imaginary dielectric permittivity using the dipolar matrix elements. Rather than using the bare output of the Yambo Fortran code, we prefer to use a simpler implementation that allows to extract contributions (see thereafter), and which faithfully reproduces the Yambo output for 1 to 12L, with a $< 3\%$ relative accuracy:

$$Im\{\varepsilon_{\alpha,\alpha}\} = \frac{e}{\hbar} \frac{16}{\Omega} \sum_{n,m,\mathbf{k}} f_{n,\mathbf{k}} (1 - f_{m,\mathbf{k}}) \times |\langle m, \mathbf{k} | \hat{r}_\alpha | n, \mathbf{k} \rangle|^2 \times Im \left\{ \frac{2(E_{m,\mathbf{k}} - E_{n,\mathbf{k}})}{(E_{m,\mathbf{k}} - E_{n,\mathbf{k}})^2 - (\omega + i\Gamma)^2} \right\} \quad (3)$$

with Ω the unit cell volume, d the cell out-of-plane extent, $f_{n\mathbf{k}}$ and $E_{n,\mathbf{k}}$ the occupation factor and energy of the $|n, \mathbf{k}\rangle$ state, and Γ the inhomogeneous broadening. The e/\hbar factor converts the expression from Hartree atomic units to SI units. From the imaginary part of the dielectric function of this unit cell of vertical extent d , we compute the in-plane real 2D optical conductivity of a single cell, normalized by the impedance of free space Z_0 , and averaged over the x, y polarizations:

$$\begin{aligned} \text{Re}\{\sigma_{2D}.Z_0\} &= d Z_0 \times \text{Re}\{\sigma\} \\ &= d \frac{1}{\varepsilon_0 c} \times \frac{1}{2} (\text{Re}\{\sigma_{x,x}\} + \text{Re}\{\sigma_{y,y}\}) \\ &= \frac{1}{2} \frac{d\omega}{c} (\text{Im}\{\varepsilon_{x,x}\} + \text{Im}\{\varepsilon_{y,y}\}) \end{aligned} \quad (4)$$

This finally leads to the expression:

$$\begin{aligned} \text{Re}\{\sigma_{2D}.Z_0\} &= \frac{16 a_0 e \omega}{\hbar c N_k} \sum_{n,m,\mathbf{k}} f_{n,\mathbf{k}} (1 - f_{m,\mathbf{k}}) \times \text{Im} \left\{ \frac{2(E_{m,\mathbf{k}} - E_{n,\mathbf{k}})}{(E_{m,\mathbf{k}} - E_{n,\mathbf{k}})^2 - (\omega + i\Gamma)^2} \right\} \\ &\quad \times \frac{1}{2} (|\langle m, \mathbf{k} | r_{x,x} | n, \mathbf{k} \rangle|^2 + |\langle m, \mathbf{k} | r_{y,y} | n, \mathbf{k} \rangle|^2) \end{aligned} \quad (5)$$

with N_k the number of \mathbf{k} -points in the unit cell surface and a_0 the Bohr radius.

From this expression one can identify the joint density of states, which is used in the main text Fig. 3c:

$$jDOS(\omega) = \frac{16}{N_k} \sum_{n,m,\mathbf{k}} f_{n,\mathbf{k}} (1 - f_{m,\mathbf{k}}) \times \text{Im} \left\{ \frac{2(E_{m,\mathbf{k}} - E_{n,\mathbf{k}})}{(E_{m,\mathbf{k}} - E_{n,\mathbf{k}})^2 - (\omega + i\Gamma)^2} \right\} \quad (6)$$

In practice, the broadening Γ is non-uniform, and we set it to increase linearly with energy ω , such that $\Gamma = 0.1 \times \omega$. The effect of broadening on the optical absorption is illustrated in Fig. 11. For the study of the many-body effects on monolayer optical conductivity in main text Fig. 4a, the broadening parameter Γ is instead set to a fixed value of 0.2 eV for simplicity.

ii. Contributions diagram

The computed real 2D optical conductivity can be inspected by displaying on the band diagram the relative contribution to the absorption of each pair of states – each n, m, \mathbf{k} (example in Fig. 12).

In practice, we use an interpolation of the \mathbf{k} -mesh to estimate the contribution to the optical absorption of each \mathbf{k} -point in the K, Γ , M and K path. The relative weights of each point is taken into account to provide a faithful representation: a single Γ is indeed shared by 12 copies of the

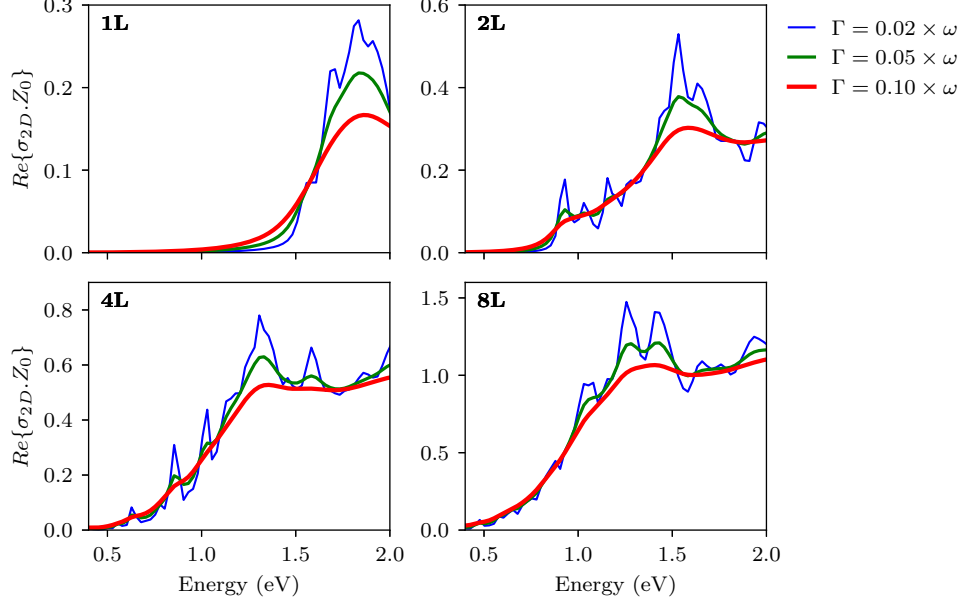


FIG. 11. Real 2D optical conductivity of 1L, 2L, 4L and 8L samples for increasing broadening $\Gamma = \{0.02, 0.05, 0.1\} \times \omega$, with ω is the energy. In-tail resonant transitions appear while the broadening is reduced.

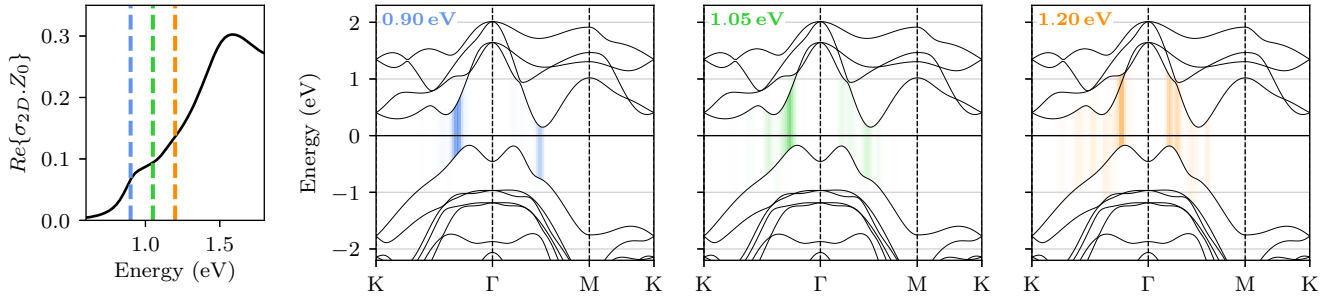


FIG. 12. Contribution diagram of the 2L 1T – PtSe₂ real 2D conductivity. At the shoulder energy of 0.9 eV, Se $p_{x/y}^+$ and Pt $d_{zx/zy}$ orbitals come into play (SM-4e).

same irreducible Brillouin zone (as pictured in main text Fig. 2a). One can note that contribution diagrams display fringed patterns, as it is the case in Fig. 12. This may be due to an oscillating phase-matching of the states involved in the dipolar coupling.

c. Further corrections applied to monolayer PtSe₂

Atomically thin two-dimensional (2D) materials host a rich set of electronic states that differ substantially from those of their bulk counterparts due to quantum confinement and enhanced many-

body effects [32]. It is known that a quantitative description of the optical response of an interacting electron system should account for electron–hole interactions. The description of these interactions goes far beyond the standard DFT scheme and the free quasiparticle picture, since electron-hole pairs can bind in bound excitons. One common approach to compute quasiparticle band structure and optical response while including electron-electron interactions and excitonic contributions is the GW plus Bethe Salpeter equation (GW-BSE), within the many body perturbation framework [30, 33–35]. This method has been applied with success to a wide variety of materials, including systems with reduced dimensionality such as MoS₂ [36], carbon nanotubes [37] and graphene [38].

i. From GGA functional to GW

Due to the well-known tendency of the semi-local exchange-correlation functional used in standard DFT (the local density (LDA) or generalized gradient (GGA) approximations, etc.) to underestimate bandgaps, we use many-body methods, by means of the quasiparticle (QP) concept (GW approximation), to correct the bandgap of the DFT band structure. Physically, the QP energies describe the energy cost of adding electrons/holes to the neutral ground state of the material. In fact, this approximation incorporates screened electron-electron correlation, which in particular permits substantial amelioration of the energy bandgaps with respect to experiments [30, 39–41].

In our work, the GW calculations is performed using the many body perturbation theory (MBPT) open-source code package Yambo [29, 30, 35, 42]. We employ the "one-shot" G_0W_0 approximation. The inverse of the microscopic dynamic dielectric function is obtained within the plasmon-pole approximation [30, 43].

We perform quasi-particle band structure simulations on a $30 \times 30 \times 1$ k-points grid using up to 200 empty bands, and we truncate exchange and correlation energies at 60 Ry and 13 Ry, respectively.

To speed up convergence with respect to empty states, we adopt the technique described in Ref [44] as implemented in the YAMBO code. We have numerically verified the convergence of the QP gap up to 50 meV with respect to the number of bands included in the calculation of both the Green and polarization functions. The Coulomb interaction is truncated in the layer-normal direction to avoid spurious interactions with the image systems. GGA and GW band diagrams are represented in Fig. 13.

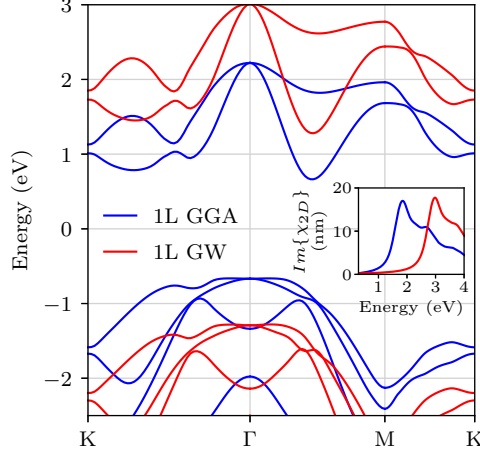


FIG. 13. Band diagrams computed with GGA-PBE and GW methods for monolayer 1T – PtSe₂. The many-body corrections result in a rigid shift of the conduction bands with respect with the valence bands, with very little modification of the bands’ profiles. In inset is plotted the 2D imaginary surface susceptibility $Im\{\chi_{2D}\} = Re\{\sigma_{2D}\} / \varepsilon_0 \omega = d(Im\{\varepsilon\} - 1)$ [10]. The bands rigid shift appears as an energy shift in susceptibility.

ii. Bethe-Salpeter Equation correction

The Bethe-Salpeter Equation (BSE) is solved using the Tamm-Dancoff approximation [42, 45] and takes into account the local field effects as implemented in yambo code [29, 30, 41]. The BSE is calculated on top of the GW eigenvalues. We obtained converged excitation energies considering, eight empty states and eight occupied states in the excitonic Hamiltonian, the irreducible BZ being sampled up to a $30 \times 30 \times 1$ k-points mesh. The same cut-offs of GW are used to build up the exchange electron-hole attractive and repulsive kernels in the BSE matrix. It is important to note that electronic transitions are very sensitive to BZ samplings. Altogether, such a treatment is much more intricate as compared to standard DFT scheme, and often restricted to systems that are small in size, due to its exceptional computational cost. For these simulation, a constant broadening of the interband transitions is used (see 4bi), of 0.2 eV.

iii. Hybrid functional HSE06

The DFT-PBE approximation often underestimates the fundamental energy band gaps due to self-interaction errors. This issue arises from the discontinuity of the chemical potential in the exchange-correlation potential, which leads to inaccuracies in the prediction of electronic band gaps

[46–48]. A manner to overcome this shortfall is to use Hybrid functional, which is extensively used to investigate a variety of periodic systems with plane wave basis sets. We shall see that the hybrid functional leads to different estimation of the band gap at the cost of a large increase in computation time. Fortunately, the relevant portion of the band structure as well as optical absorption are strongly similar to GGA.

Among the several proposed hybrid functional (PBE0 [49], B3LYP [50], HSE [51] etc.), in our work we will use the Heyd-Scuseria-Ernzerhof functional (HSE06), which is often used to compute the electronic properties of layered materials. HSE06 is a type of exchange-correlation functional which combines the KS orbitals (GGA/LDA) with a portion of exact Hartree-Fock (HF) exchange. Specifically, HSE06 splits the exchange interaction into short-range and long-range components, applying the HF exchange only to the short-range part and using a GGA-like exchange for the long-range part [51, 52].

The electronic structure calculations were carried out using the hybrid functional HSE06 implemented in QE [11–13]. The HSE06 functional incorporates 25% exact HF exchange. For the plane-wave basis set, a cutoff energy of $60R_y$ for the wavefunctions and a k-point grid of $15 \times 15 \times 1$ for Brillouin zone was used. The q-grid dimensions for the HF exchange interaction were set to $10 \times 10 \times 1$. These parameters are crucial for ensuring the convergence of the HF exchange interaction in HSE06 calculations, which directly impacts the accuracy of the hybrid functional results. However, increasing these q-grid dimensions can significantly raise the computational cost, as it requires more extensive calculations to accurately capture the exchange interactions. Wannier90 [53, 54] was then used to project the electronic states onto localized Wannier functions and to map band structure energies from k-grid-based calculations onto finely spaced k-paths by means of Wannier interpolation.

The electronic band structure using GGA and HSE functional for 1ML PtSe₂ are presented in Figure 14. The indirect band gap values determined by the Wannier-interpolated HSE06 band structure is increased by 0.5 eV as compared to GGA approximation, besides, the band structure is unchanged in the band edges of CBM and VBM. Computationally, using HSE06 is more demanding than GGA due to the need to compute the exact exchange integrals, which require a non-local treatment of the electron-electron interaction. This increases the computational cost and complexity, often necessitating more sophisticated algorithms and longer computation times, particularly for multilayer cases. Therefore, in the main text we choose to use the GGA approximation.

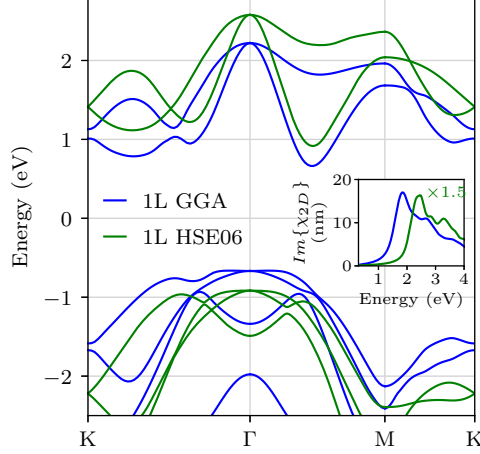


FIG. 14. Band diagrams computed with GGA-PBE and HSE06 methods for monolayer 1T – PtSe₂. In inset is plotted the imaginary surface susceptibility $Im\{\chi_{2D}\} = Re\{\sigma_{2D}\} / \varepsilon_0\omega = d(Im\{\varepsilon\} - 1)$ [10].

iv. Finite temperature optical absorption

To explore the role of phonons in the optical absorption spectrum and the band-gap renormalization, we employed the method of special displacements implemented in the *ZG.x* code within EPW [55]. This nonperturbative approach involves computing the band structure and optical spectra at each temperature using a sufficiently large supercell. The atomic positions in this supercell are appropriately distorted according to the phonon displacement patterns calculated using density-functional perturbation theory (DFPT). Below, we summarize the calculation procedure and convergence parameters. A detailed description can be found in the following references [55–57]

(i) Using DFPT module of Quantum Espresso, We determine the interatomic force constants in the primitive unit cell, using a uniform grid of $8 \times 8 \times 1$ q-points. By diagonalizing the dynamical matrix obtained from the matrix of force constants, we determine the phonon eigenmodes $e_{\kappa\alpha,\nu}(\mathbf{q})$ and eigenfrequencies $\omega_{\mathbf{q}\nu}$ (κ and α indicate the atom and the Cartesian direction, respectively) used to construct the Zacharias Guistino (ZG) displacement. The reliable determination of ZG displacement requires the knowledge phonon-band dispersion with an accuracy on the order of 0.1 meV. Therefore, we perform the DFPT calculation with a high cutoff energy of $100R_y$.

(ii) In preparation for calculations on a supercell of size $8 \times 8 \times 1$, we interpolate the vibrational eigenmodes and frequencies on a finer q-points grid with the same size as the supercell, then at each temperature, a $8 \times 8 \times 1$ supercell of 179 atoms is constructed starting from the real-space force constants, by using the *ZG code* that is part of EPW open source package [55].

(iii) To compute band structures, we first set up the k-point path in the Brillouin zone of the primitive cell, then we obtain the folded k-points in the Brillouin zone of the supercell. We perform a DFT band structure calculation in the supercell, and we unfold the result using the method of Ref. [58]. Supercell GGA calculations are performed with wavefunction cutoff of $80R_y$.

(iv) To obtain temperature-dependent optical absorption spectra, steps (i)–(ii) above remain the same, while step (iii) is replaced by the calculation of the optical matrix elements in the independent particle approximation (IPA).

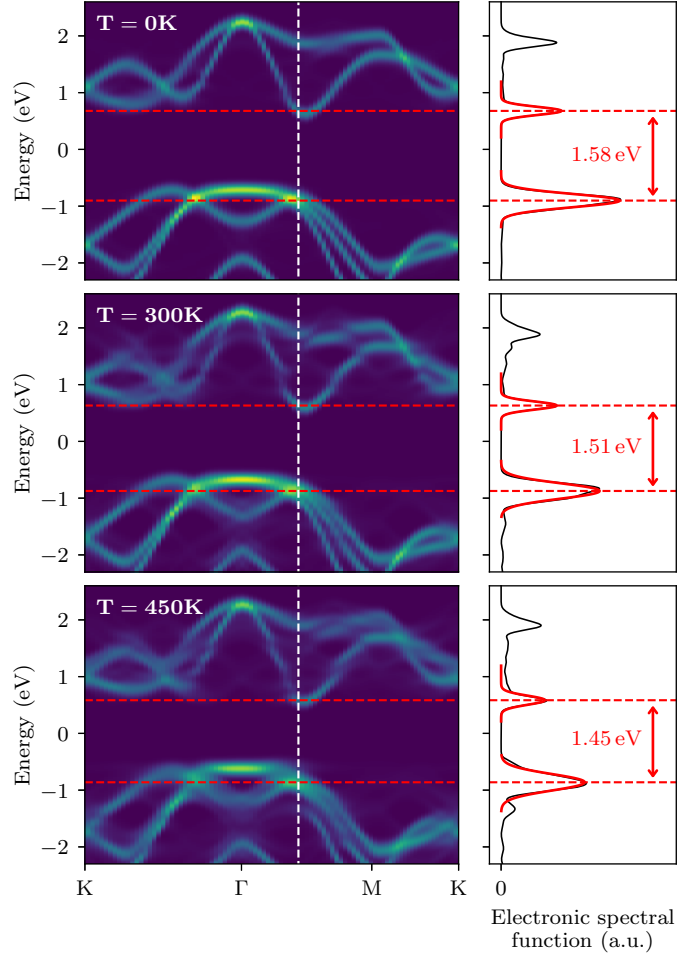


FIG. 15. (left) Spectral function of ML PtSe₂ calculated using the special displacement method as implemented in the ZG code at $T = 0\text{ K}$, 300 K and 450 K . (right) Spectral function at the direct bandgap \mathbf{k} wavevector (dashed white line in the left panel). The direct bandgap value is extracted in between the conduction and valence bands using Gaussian fitting of the spectral function.

To assess the role of temperature renormalization of the electronic band structure, which may induce a shift of the bands and can be mistaken for an effect of the indirect transitions, we plot in Fig. 15 the spectral function of PtSe₂ for three different temperatures $T = 0\text{ K}$, 300 K and 450 K

obtained from the ZG displacement [57] in a $8 \times 8 \times 1$ supercell.

By extracting the corresponding direct temperature-dependent bandgap, we find that it decreases from 1.58 eV at $T = 0$ K to 1.45 eV at $T = 450$ K. This confirms a renormalization effect (redshift) with temperature, that explains the small redshift of the optical absorption tail observed in the temperature-dependent simulations (main text Fig. 3a). This allows us to definitively exclude phonon-assisted indirect transitions as the main cause of the observed experimental absorption tail.

d. AB stacked bilayers

Stacking of the sublayers in a layered material directly affect its electronic and optical properties. Different stackings of 2L PtSe₂ can theoretically be obtained through layer shifting and/or rotation at various angles. In our case, we will study three possible stackings, namely AA, AB₁ and AB₂. The AA stacking is the most stable form of 2L PtSe₂ (used in main text Fig. 1), it corresponds to the stacking order of bulk PtSe₂. In this structure, the Pt atoms are aligned vertically. The AB₁ structure's is obtained by rotating the upper layer of AA PtSe₂ by 180° around the Pt atom. The AB₂ structure is obtained by translating the upper layer of the AB₁ structure in the direction of $\mathbf{a} - \mathbf{b}$ with a magnitude of $|\mathbf{a} - \mathbf{b}|/3$. After constructing AB₁ and AB₂ stacking both are fully relaxed on both the lateral cell constants and ion positions based on DFT as implemented in QE (see section 4a). These bilayer PtSe₂ calculations are based on the work of reference [59].

	AA	AB ₁	AB ₂
a (Å)	3.74	3.69	3.71
d_{pt-pt} (Å)	5.17	6.42	5.38
ΔE_B (meV)	-322	-286	-282

TABLE II. Optimized lattice parameter a , Pt-Pt distance d_{Pt-Pt} , and binding energy ΔE_B for different stackings 2L PtSe₂.

In table 4d, we display the lattice constant, the interlayer distance d_{Pt-Pt} and the Binding energy ΔE_B for the three mentioned structure. As expected, we find that the top-to-top (AA) arrangement is energetically the most stable stacking of 1T-PtSe₂ layers. In Fig. 16, we plot their band structure.

Different stackings could effectively modulate the band structures of bilayer PtSe₂. The AA structure has the minimum bandgap of 0.3 eV and the larger interlayer distance, while the corresponding AB₁ – which has the lower interlayer distance – has a bandgap almost two times larger.

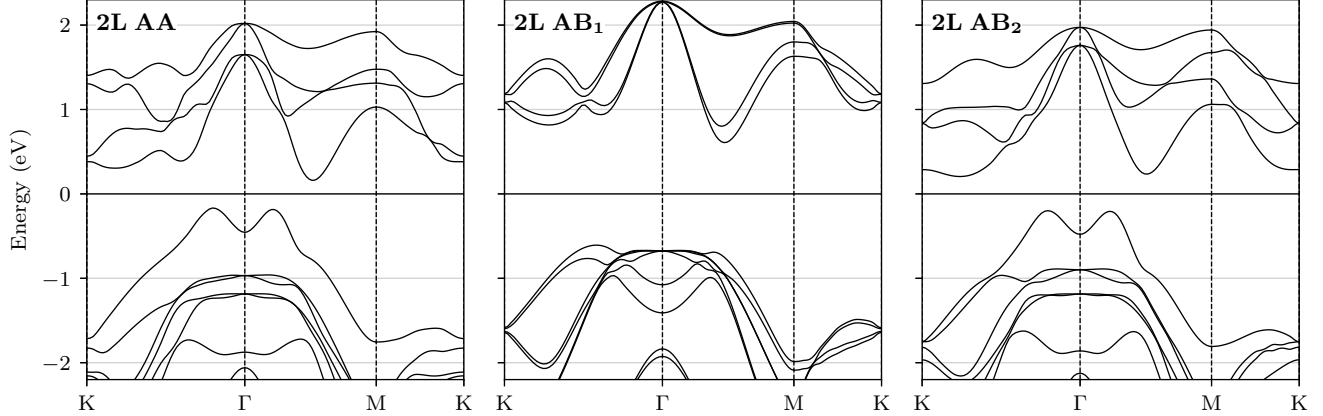


FIG. 16. Band diagrams computed with the GGA method for 2L with AA, AB₁ and AB₂ stacked 1T – PtSe₂.

e. Orbital projected partial density of states

i. Simulation method

In order to identify the contribution of the different atomic orbitals to the electronic band structure and hence to the optical absorption spectra, we calculate the projected density of states (PDOS) by projecting the wave-functions onto the localized atomic orbitals. Such a calculation is done using the Projector Augmented Wave (PAW) method, as implemented in Quantum Espresso’s through projwfc.x code. A PAW pseudopotential, denser k point $40 \times 40 \times 1$ and the tetrahedron method with Blöchl’s correction was used [11–13].

ii. Orbitals projections

We investigate the electronic state projection onto the localized atomic orbitals. To do so, we monitor the valence states of the Selenium atoms 4s and 4p, and those of the Platinum atoms 5d, 6s and 6p. The orbitals components displayed thereafter are the projection coefficients modulus squared obtained from the PDOS method.

The Se p and the Pt d orbitals are dominating the band diagram around the bandgap energy region, as displayed in Fig. 17a, for the case of a monolayer. The Pt d orbital can be decomposed further in d_{z^2} , $d_{zx/zy}$, $d_{x^2-y^2/xy}$ harmonics (Fig. 17b), for which we gather the atomic orbitals in three groups accounting for Z -rotation symmetry, due to the unpolarized light in our problem. The Se p orbital can likewise be decomposed in p_z and $p_{x/y}$ harmonics. However there are two Selenium

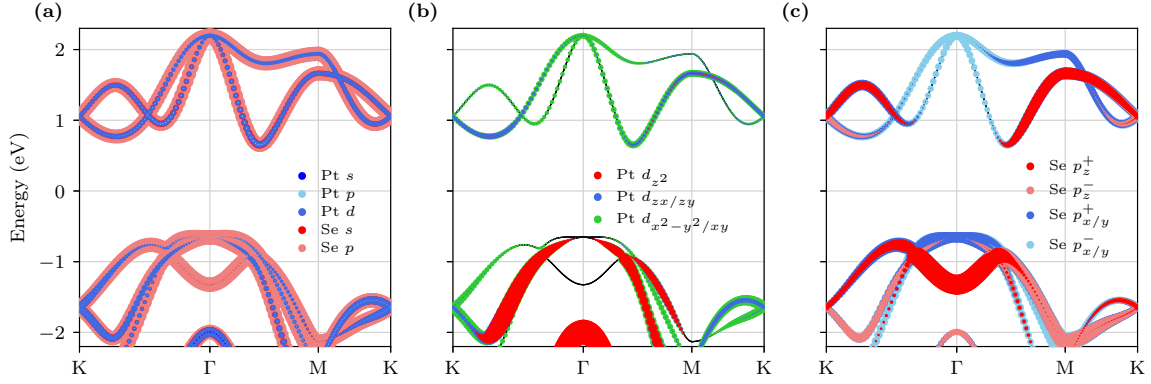


FIG. 17. Projection of the electronic wavefunction of 1L PtSe₂ on localized atomic orbitals of (a) Platinum and Selenium atoms, (b) d orbitals of the Platinum atom, (c) the p orbitals of the Selenium atoms, in symmetric and antisymmetric combinations.

atoms per unit cell, and one can consider symmetric and antisymmetric combinations of the two states, thereafter labeled $+/-$ (Fig. 17c).

iii. Orbitals decomposition of optical transitions

We want to assess the coupling strength between these orbitals to understand the features of the optical absorption computed in our study. To estimate the coupling of orbitals, we use a procedure similar to the Slater Koster calculation of interatomic elements for tight-binding models [60]. This coupling is evaluated by the square of the dipolar matrix elements, as in the equation:

$$|\langle \Psi_1 | \mathbf{p} | \Psi_2 \rangle|^2 = \left| -i\hbar \cdot \int d\mathbf{r} \Psi_1(\mathbf{r})(\nabla \Psi_2(\mathbf{r})) \right|^2 \quad (7)$$

To be non-zero, the electromagnetic interaction has to involve orbitals of different parities (excluding Se p - Se p interaction for instance), Pt d and Se p coupling having therefore the prominent contribution. We evaluate numerically the coupling of each Platinum d orbital harmonics with the p orbital harmonics of the 6 neighboring Selenium atom by using for the atomic states the following ansatz:

$$\Psi_1(\mathbf{r}) \sim r^l e^{-r/d} Y_{l,m}(\theta, \phi) \quad (8)$$

where l and m are the azimuthal and magnetic quantum numbers, $Y_{l,m}$ the associated spherical harmonic and $d = 0.5 a_0$ is the controlling the radial range (a_0 is the Bohr radius), chosen such that

the orbitals spread is typically on the order of the distance between the Se and Pt planes (illustrated in Fig. 18).

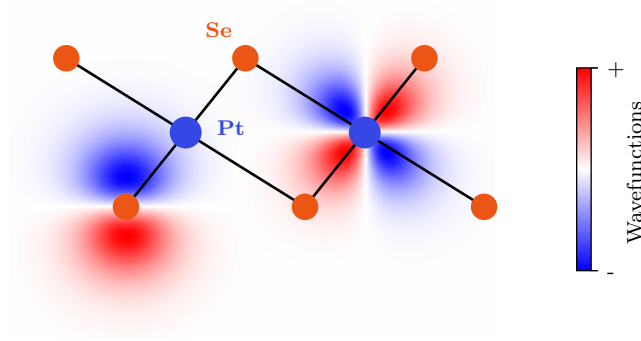


FIG. 18. Se p_z (left) and Pt d_{zy} (right) orbitals ansatz, represented in the yz plane, at the atomic positions, with $d = 0.5 a_0$.

Orbitals	x polarization			y polarization		
	Se p_{z+}	Se p_{x+}	Se p_{y+}	Se p_{z+}	Se p_{x+}	Se p_{y+}
Pt d_{z^2}	0	0.15	0	0	0	0.15
Pt d_{zx}	0.21	0	1.00	0	1.00	0
Pt d_{zy}	0	1.00	0	0.21	0	1.00
Pt $d_{x^2-y^2}$	0	0.01	0	1.00	0	0.01
Pt d_{yx}	1.00	0	0.01	0	0.01	0

TABLE III. Coupling Selenium and Platinum orbitals in arbitrary units. x is being chosen along the main crystallographic axis. x and y polarizations couple complementary orthogonal orbitals with the same intensity, in agreement with the definitions of Pt d_{z^2} , $d_{zx/zy}$, $d_{x^2-y^2/xy}$ and Se p_{z+} , $p_{x/y}^+$ orbitals groups to account for unpolarized light. Asymmetric combinations of Se p orbitals were found to present a zero coupling with Pt d orbitals.

We find that the couplings involving an antisymmetric combination of Selenium P orbitals are zero, which relies on crystal symmetries. The couplings involving its symmetric part are detailed in **table III**, for either x or y light polarization. The computed values are indicative, and vary with the ansatz range of the atomic wavefunction. Nonetheless two dominating couplings are systematically standing out, with equal intensities: Pt $d_{zx/zy}$ and Se $p_{x/y}^+$ on one hand, and Pt $d_{x^2-y^2/xy}$ and p_{z+} on the other hand. This justifies that we only consider the couplings of these orbitals as the principal

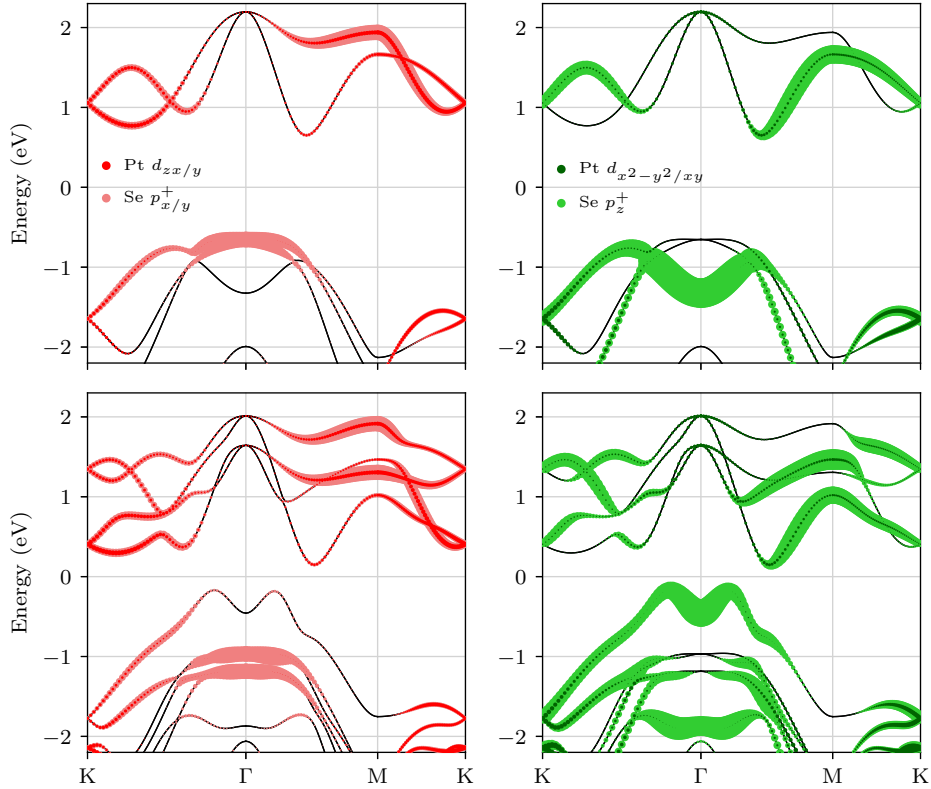


FIG. 19. Orbital decomposition of the main orbitals which coupling is responsible for the optical absorption: (left) Pt $d_{zx/zy}$ and Se $p_{x/y}^+$, and (right) Pt $d_{x^2-y^2/xy}$ and p_z^+ , for (top) monolayer and (bottom) bilayer PtSe₂.

source of optical absorption. The wavefunctions projections on these orbitals are consequently drawn in Fig. 19, for the cases of 1L and 2L.

5. DENSITY OF STATES, PEAKS AND LOW-ENERGY SCALING

a. Optical absorption and $jDOS$

We come back to the nature of the absorption peaks, by inspecting the joint density of states. We already know that the dipolar couplings responsible for the absorption vary smoothly around the region of the Brillouin zone involved in the peak's optical absorption (Fig. 19), and are thus unlikely to be the cause of such maxima. To confirm that the optical absorption peaks are indeed due to the band nesting effect, we check that these peaks are present in the joint density of states. We compare the real 2D optical conductivity and the $jDOS$ times frequency ($\sigma_{2D} \sim \omega \cdot M \cdot jDOS$ where M is the dipolar coupling, see section 4bi), for 1L and 2L PtSe₂ (Fig. 20 top).

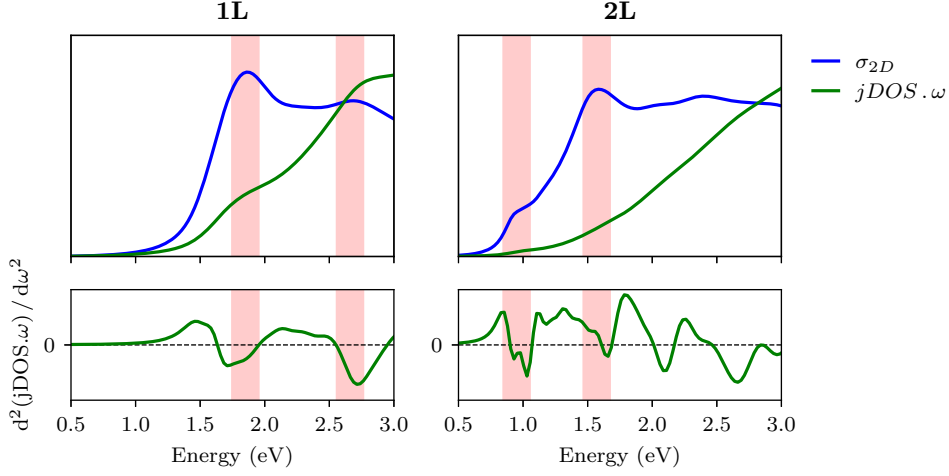


FIG. 20. Absorption peaks and $jDOS$. (top) Simulated real 2D optical conductivity and joint density of states $jDOS$, and (bottom) $jDOS$ curvature, for (left) monolayer and (right) bilayer stackings. In red are highlighted the main peaks energies: 1.85 eV and 2.66 eV for 1L, 0.95 eV and 1.57 eV for 2L.

If some shoulders are visible in the 1L $jDOS$, corresponding to the main peaks, they are hardly noticeable for the 2L. This is because the multiplicity of the bands average out the contributions to form a smoothly increasing function. We prefer to take the second derivative of $\omega \cdot jDOS$ in order to distinguish the most-pronounced local maxima (they appear as minima of the double derivative, see Fig. 20 bottom). We can distinguish the two main peaks for 1L, and the main peak for the 2L as well as its small peak located in the absorption tail. However it is hard to conclude for the 2L second absorption peak, since several transitions come into play.

b. Low-energy scaling law

To understand how to extract a scaling from the energy bands' landscape to estimate the optical absorption tail, let's first recall that the 2D optical conductivity σ_{2D} and the joint density of states $jDOS$ can be obtained using sums over the band diagram:

$$\sigma_{2D}(\omega) \sim \sum_{c,v} \int_{\mathbf{k}} d^3\mathbf{k} M_{k,c,v} \delta[\omega - (E_{c,\mathbf{k}} - E_{v,\mathbf{k}})] \quad (9)$$

$$jDOS(\omega) \sim \sum_{c,v} \int_{\mathbf{k}} d^3\mathbf{k} \delta[\omega - (E_{c,\mathbf{k}} - E_{v,\mathbf{k}})] \quad (10)$$

where ω is the frequency, c and v designate the conduction and valence bands indices and $M_{k,c,v}$ is the dipolar matrix element. We omitted here the Pauli blocking term for partially filled bands.

We consider the bulk limit: while the 2D confined model implies a band degeneracy lift upon stacking, we consider here that we operate instead in the continuous k_z limit. In this picture, the transitions between multiple bands responsible for the low energy absorption tail reduce to transitions between a single pair of bands. The evolution of this coupling is represented along the absorption tail with a contribution diagram in Fig. 21.

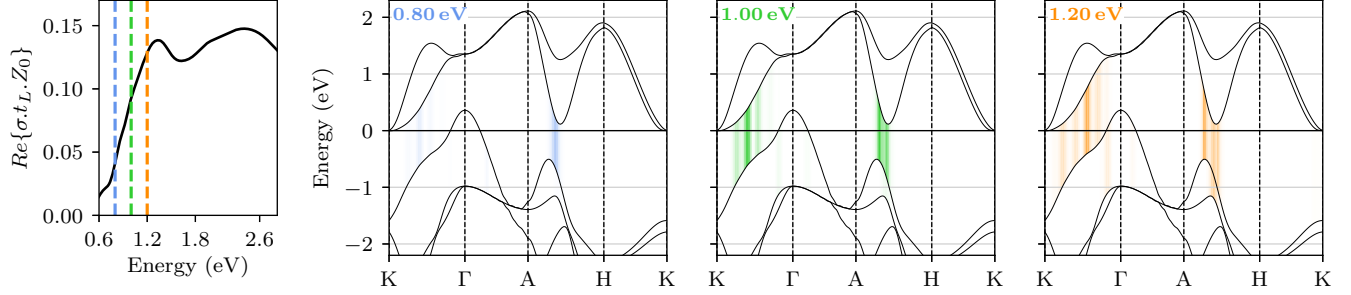


FIG. 21. Contribution diagram of the PtSe₂ bulk single layer 2D real optical conductivity σ_{tL} (σ is the bulk conductivity, t_L is the layer thickness). The diagram is restricted to the K, Γ , A and H points where are located the contributing transitions

We consider a quadratic energy dependency of the electronic transitions involved in the optical absorption, close to the minimum energy: $\omega - \omega_0 \sim (\mathbf{k} - \mathbf{k}_0)^2$. We consequently find for the $jDOS$ the standard 3D density of states scaling with frequency:

$$\begin{aligned}
 jDOS(\omega) &\sim \int d^3\mathbf{k} \delta[\omega - E(\mathbf{k})] \\
 &\sim \int k^2 dk \delta[\omega - E(\mathbf{k})] \\
 &\sim \int dE \sqrt{E - \omega_0} \delta[\omega - E] \\
 &\sim \sqrt{\omega - \omega_0}
 \end{aligned} \tag{11}$$

If a single transition is involved then we can consider a constant dipolar matrix element M and use equation (11), raising $Re\{\sigma_{2D}\} \sim \omega \cdot M \cdot jDOS(\omega) \sim \omega \sqrt{\omega - \omega_0}$. From this dependency one can deduce a linear law to extrapolate from the 2D real optical conductivity the energy ω_0 of the optical transition involved:

$$\left(\frac{Re\{\sigma_{2D}\}}{\omega} \right)^2 \sim \omega - \omega_0 \tag{12}$$

c. Rigid shift hypothesis

The hypothesis of a rigid shift of the electronic bands dispersion allows us to correct for the GGA indirect bandgap (Fig. 4 in the main text). We now justify this hypothesis by comparing the outcome of different DFT simulations: the GGA method, on which our work is mainly based, as well as GW and HSE methods (sections 4ci and 4ciii). To do so, we apply a rigid shift in between the valence and conduction bands of the GW and HSE06 bands dispersion to set their indirect bandgap value to the one found with the GGA method (Fig. 22).

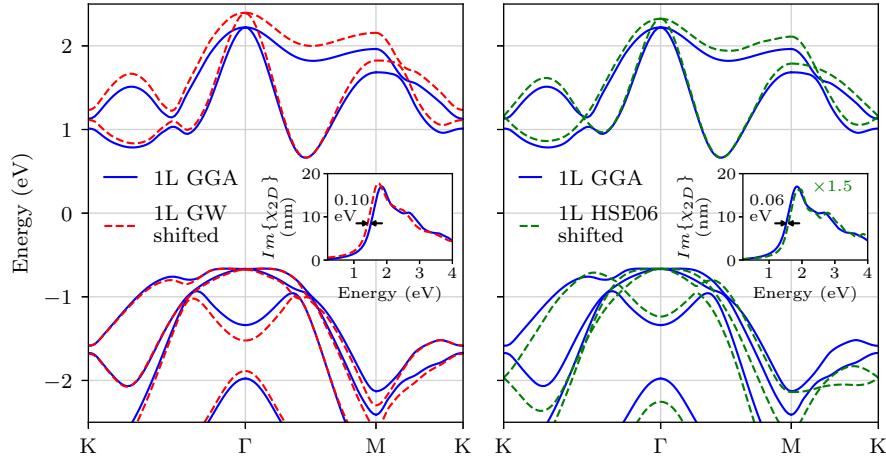


FIG. 22. Electronic bands dispersion computed with GGA, GW and HSE06 methods (see section 4a). The GW and HSE06 bands are rigidly shifted in order to match the bandgap of the GGA bands dispersion. In inset are represented the imaginary surface susceptibility $Im\{\chi_{2D}\} = Re\{\sigma_{2D}\} / \epsilon_0 \omega = d(Im\{\epsilon\} - 1)$ where the same shifts are applied. A residual -0.10 eV shift of the absorption tail for the GW method and of $+0.06$ eV for the HSE06 tail are present with respect to the GGA absorption tail.

Comparing the band diagram, we find that the conduction band and the valence band in the vicinity of the Γ point appear to be rigidly shifted, but relative distortions can indeed be observed, in particular close to the edge of the first Brillouin zone (M-K). These distortions have a negligible impact on optical absorption near the direct bandgap, which justifies to neglect them for the study of the near-infrared absorption tail.

We evaluate the accuracy of the rigid shift hypothesis by evaluating the direct and indirect bandgaps for each method, as well as evaluating their difference (see table IV). We find that the energy difference between direct and indirect bandgaps obtained with the various DFT methods are consistent within a 60 meV spread.

DFT method	Direct bandgap (eV)	Indirect bandgap (eV)	Difference (eV)
GGA	1.53	1.33	0.20
GW	2.79	2.56	0.23
HSE06	2.00	1.83	0.17

TABLE IV. Direct, indirect bandgaps and differences for GGA, GW and HSE06 DFT methods.

Examining now the optical absorption tail simulated by the different methods (Fig. 22), the shifted GW tail features a remaining -0.10 eV shift of the absorption tail with respect to the GGA tail. This shift is of $+0.06$ eV in between the shifted HSE06 optical absorption tail and the GGA-simulated one. As the GW method features a large bandgap shift (2 eV) compared to the experimentally extracted one, we consequently expect that this large shift also leads to larger distortions.

As a consequence, we consider that the characteristic accuracy of the indirect bandgap extraction method used in the main text is of 60 meV. This a small value against the total bandgap shift (0.33 eV). As the indirect bandgap shifts by about ~ 50 meV/layer for a thickness of 7 layers, this typical error translates to an estimation range of the semiconductor-to-semimetal transition thickness of 6 to 8 layers.

6. PHOTOLUMINESCENCE OF EXFOLIATED FLAKES

Photoluminescence is investigated at room temperature, on the visible (1.2 – 2.5 eV) range, in order to evaluate the presence of a possible bound exciton in the absorption profile.

A 0.4 mW 532 nm green laser light is focused onto selected samples, using a $\times 80$ microscope objective. Photoluminescence from the flake under study and the nearby substrate are collected – the latter being used as a reference. The measured signal is normalized by the collection efficiency at 570 nm and corrected for the CCD and diffraction grating spectral efficiencies. The resulting data is displayed Fig. 23, for 1L, 2L, 4L and 8L samples.

The measured signal is extremely low, with a total yield below 10^{-7} , pointing to a very inefficient effect. The spectral profile for 2L, 3L and 8L sample feature wide bumps around 1.3–1.5 eV, and the one of 1L appears rather flat (the discontinuity at 1.4 eV is an experimental artefact). These broad photoluminescence peaks can hardly be attributed to excitonic features, but probably originate from some substrate’s contamination photoluminescence, exacerbated by the PtSe₂ absorption at

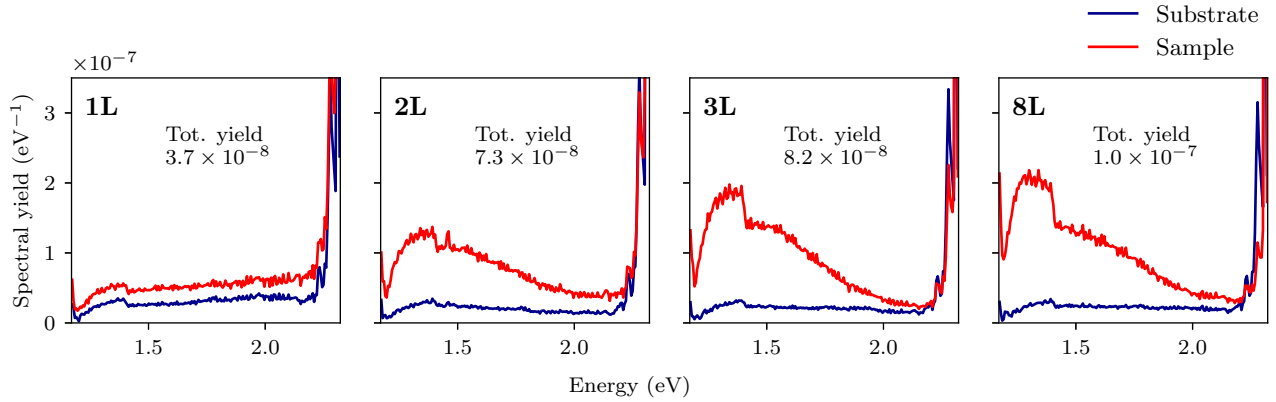


FIG. 23. Photoluminescence signal collected from 1L, 2L, 3L and 8L samples and from the substrate at their vicinity, on the 1.2 – 2.3 eV range. The signal is normalized and binned as a spectral yield (in unit of eV^{-1}), and sums up to a total yield, displayed for each sample. The step at 1.4 eV is arising from the use of two different spectral windows

the interface.

7. AUTHORS CONTRIBUTIONS

MT, RLG, CV and EB designed the experiments with the help of PM. MT conducted the sample fabrication with the help of RLG, JP and MR. MT performed the optical spectroscopy measurements and analysis. SA and MA performed the DFT simulations and atomic orbital projection with the help of RF and FC. SA, MA, and MT computed the optical properties. MT computed the atomic orbital couplings. MT and ED performed the Raman spectroscopy. ED and PL grew the MBE thin film. MT, SA, RLG, BP, FC, CV, RF and EB developed the theoretical interpretation. MT and EB wrote the manuscript with contributions from the coauthors.

-
- [1] S. B. Desai, S. R. Madhvapathy, M. Amani, D. Kiriya, M. Hettick, M. Tosun, Y. Zhou, M. Dubey, J. W. Ager III, D. Chrzan, and A. Javey, *Advanced Materials* **28**, 4053 (2016).
- [2] M. Heyl, D. Burmeister, T. Schultz, S. Pallasch, G. Ligorio, N. Koch, and E. J. W. List-Kratochvil, *physica status solidi (RRL) – Rapid Research Letters* **14**, 2000408 (2020).
- [3] M. Tharrault, E. Desgué, D. Carisetti, B. Plaçais, C. Voisin, P. Legagneux, and E. Baudin, *2D Materials* **11**, 025011 (2024).

- [4] On the XRD measurement of reference [61], the first diffraction peak being at $2\theta = 17.51^\circ$ for $\lambda = 1.541\text{\AA}$, one can infer the c-axis parameter as $\lambda/(2\sin(\theta)) = 0.506\text{ nm}$.
- [5] K. M. McPeak, S. V. Jayanti, S. J. P. Kress, S. Meyer, S. Iotti, A. Rossinelli, and D. J. Norris, *ACS Photonics* **2**, 326 (2015).
- [6] I. H. Malitson, *J. Opt. Soc. Am.* **55**, 1205 (1965).
- [7] G. A. Ermolaev, K. V. Voronin, M. K. Tatmyshevskiy, A. B. Mazitov, A. S. Slavich, D. I. Yakubovsky, A. P. Tselin, M. S. Mironov, R. I. Romanov, A. M. Markeev, I. A. Kruglov, S. M. Novikov, A. A. Vyshnevyy, A. V. Arsenin, and V. S. Volkov, *Nanomaterials* **11**, 3269 (2021).
- [8] M. A. Green, *Solar Energy Materials and Solar Cells* **92**, 1305 (2008).
- [9] K. Kolwas and A. Derkachova, *Nanomaterials* **10**, 10.3390/nano10071411 (2020).
- [10] Y. Li and T. F. Heinz, *2D Materials* **5**, 025021 (2018).
- [11] W. Kohn and L. J. Sham, *Phys. Rev.* **140**, A1133 (1965).
- [12] P. Giannozzi, S. Baroni, N. Bonini, M. Calandra, R. Car, C. Cavazzoni, D. Ceresoli, G. L. Chiarotti, M. Cococcioni, I. Dabo, *et al.*, *Journal of Physics: Condensed Matter* **21**, 395502 (2009).
- [13] P. Giannozzi, O. Andreussi, T. Brumme, O. Bunau, M. B. Nardelli, M. Calandra, R. Car, C. Cavazzoni, D. Ceresoli, M. Cococcioni, *et al.*, *Journal of Physics: Condensed Matter* **29**, 465901 (2017).
- [14] J. P. Perdew, K. Burke, and M. Ernzerhof, *Phys. Rev. Lett.* **77**, 3865 (1996).
- [15] M. van Setten, M. Giantomassi, E. Bousquet, M. Verstraete, D. Hamann, X. Gonze, and G.-M. Rignanese, *Computer Physics Communications* **226**, 39 (2018).
- [16] S. Grimme, *Journal of Computational Chemistry* **25**, 1463 (2004).
- [17] S. Grimme, J. Antony, S. Ehrlich, and H. Krieg, *The Journal of Chemical Physics* **132**, 154104 (2010).
- [18] T. Thonhauser, S. Zuluaga, C. A. Arter, K. Berland, E. Schröder, and P. Hyldgaard, *Phys. Rev. Lett.* **115**, 136402 (2015).
- [19] A. Tkatchenko and M. Scheffler, *Phys. Rev. Lett.* **102**, 073005 (2009).
- [20] A. Jain, S. P. Ong, G. Hautier, W. Chen, W. D. Richards, S. Dacek, S. Cholia, D. Gunter, D. Skinner, G. Ceder, and K. A. Persson, *APL Materials* **1**, 011002 (2013).
- [21] T. H. Fischer and J. Almlof, *The Journal of Physical Chemistry* **96**, 9768 (1992).
- [22] H. J. Monkhorst and J. D. Pack, *Phys. Rev. B* **13**, 5188 (1976).
- [23] C. Lee, W. Yang, and R. G. Parr, *Phys. Rev. B* **37**, 785 (1988).
- [24] G. Y. Guo and W. Y. Liang, *Journal of Physics C: Solid State Physics* **19**, 995 (1986).

- [25] K. Zhang, M. Yan, H. Zhang, H. Huang, M. Arita, Z. Sun, W. Duan, Y. Wu, and S. Zhou, *Phys. Rev. B* **96**, 125102 (2017).
- [26] A. Kandemir, B. Akbali, Z. Kahraman, S. V. Badalov, M. Ozcan, F. Iyikanat, and H. Sahin, *Semiconductor Science and Technology* **33**, 085002 (2018).
- [27] P. Li, L. Li, and X. C. Zeng, *Journal of Materials Chemistry C* **4**, 3106 (2016).
- [28] Y. Wang, L. Li, W. Yao, S. Song, J. T. Sun, J. Pan, X. Ren, C. Li, E. Okunishi, Y.-Q. Wang, E. Wang, Y. Shao, *et al.*, *Nano Letters* **15**, 4013 (2015).
- [29] A. Marini, C. Hogan, M. Grüning, and D. Varsano, *Computer Physics Communications* **180**, 1392 (2009).
- [30] D. Sangalli, A. Ferretti, H. Miranda, C. Attaccalite, I. Marri, E. Cannuccia, P. Melo, M. Marsili, F. Paleari, A. Marrazzo, *et al.*, *Journal of Physics: Condensed Matter* **31**, 325902 (2019).
- [31] *Yambo cheatsheet 5.0*, Tech. Rep. (Yambo project, April 2021).
- [32] K. S. Thygesen, *2D Materials* **4**, 022004 (2017).
- [33] G. Onida, L. Reining, and A. Rubio, *Rev. Mod. Phys.* **74**, 601 (2002).
- [34] M. S. Hybertsen and S. G. Louie, *Phys. Rev. B* **34**, 5390 (1986).
- [35] G. Strinati, *La Rivista del Nuovo Cimento (1978-1999)* **11**, 1 (1988).
- [36] D. Y. Qiu, F. H. da Jornada, and S. G. Louie, *Phys. Rev. Lett.* **111**, 216805 (2013).
- [37] C. D. Spataru, S. Ismail-Beigi, L. X. Benedict, and S. G. Louie, *Phys. Rev. Lett.* **92**, 077402 (2004).
- [38] L. Yang, J. Deslippe, C.-H. Park, M. L. Cohen, and S. G. Louie, *Phys. Rev. Lett.* **103**, 186802 (2009).
- [39] T. Rangel, M. Del Ben, D. Varsano, G. Antonius, F. Bruneval, F. H. da Jornada, M. J. van Setten, O. K. Orhan, D. D. O'Regan, A. Canning, *et al.*, *Computer Physics Communications* **255**, 107242 (2020).
- [40] M. van Schilfgaarde, T. Kotani, and S. Faleev, *Phys. Rev. Lett.* **96**, 226402 (2006).
- [41] A. Guandalini, P. D'Amico, A. Ferretti, and D. Varsano, *npj Computational Materials* **9**, 44 (2023).
- [42] G. Onida, L. Reining, and A. Rubio, *Rev. Mod. Phys.* **74**, 601 (2002).
- [43] P. Larson, M. Dvorak, and Z. Wu, *Phys. Rev. B* **88**, 125205 (2013).
- [44] F. Bruneval and X. Gonze, *Phys. Rev. B* **78**, 085125 (2008).
- [45] S. M. Dancoff, *Phys. Rev.* **78**, 382 (1950).
- [46] J. Heyd, J. E. Peralta, G. E. Scuseria, and R. L. Martin, *The Journal of chemical physics* **123** (2005).
- [47] J. P. Perdew and K. Burke, *International journal of quantum chemistry* **57**, 309 (1996).
- [48] L. J. Sham and M. Schlüter, *Physical review letters* **51**, 1888 (1983).
- [49] J. P. Perdew, M. Ernzerhof, and K. Burke, *The Journal of chemical physics* **105**, 9982 (1996).

- [50] A. D. Becke, Physical review A **38**, 3098 (1988).
- [51] J. Heyd, G. E. Scuseria, and M. Ernzerhof, The Journal of chemical physics **118**, 8207 (2003).
- [52] A. D. Becke, The Journal of chemical physics **98**, 1372 (1993).
- [53] N. Marzari, A. A. Mostofi, J. R. Yates, I. Souza, and D. Vanderbilt, Reviews of Modern Physics **84**, 1419 (2012).
- [54] G. Pizzi, V. Vitale, R. Arita, S. Blügel, F. Freimuth, G. Géranton, M. Gibertini, D. Gresch, C. Johnson, T. Koretsune, *et al.*, Journal of Physics: Condensed Matter **32**, 165902 (2020).
- [55] S. Poncé, E. R. Margine, C. Verdi, and F. Giustino, Computer Physics Communications **209**, 116 (2016).
- [56] M. Zacharias and F. Giustino, *Phys. Rev. Res.* **2**, 013357 (2020).
- [57] M. Zacharias and F. Giustino, *Phys. Rev. B* **94**, 075125 (2016).
- [58] V. Popescu and A. Zunger, Physical Review B—Condensed Matter and Materials Physics **85**, 085201 (2012).
- [59] L. Fang, W. Liang, Q. Feng, and S.-N. Luo, *Journal of Physics: Condensed Matter* **31**, 455001 (2019).
- [60] J. C. Slater and G. F. Koster, *Phys. Rev.* **94**, 1498 (1954).
- [61] Hq graphene - ptse2, <https://www.hqgraphene.com/PtSe2.php> (2021).